An adaptive estimation approach based on fisher information to overcome the flat voltage plateau challenges of SOC estimation in LFP batteries

Energy and AI 24 (2026) 100693

Contents lists available at ScienceDirect

Energy and AI

journal homepage: www.sciencedirect.com/journal/energy-and-ai

An adaptive estimation approach based on fisher information to overcome the flat voltage plateau challenges of SOC estimation in LFP batteries

Junzhe Shi [a], Shida Jiang [a], Shengyu Tao [a,b,*], Jaewong Lee [a], Manashita Borah [a,c], Scott Moura [a]

[a] University of California, Systems Engineering, 760 Davis Hall, Berkeley, CA 94720, USA
[b] Department of Electrical Engineering, Chalmers University of Technology, Gothenburg 41296, Sweden
[c] Tezpur University, Department of Electrical Engineering, Assam 784028, India

HIGHLIGHTS

- Real-time Fisher information guides confidence-weighted SOC fusion.
- Robust SOC estimation immune to current bias and flat OCV-SOC zones.
- 3D OCV-Hysteresis-SOC map enables real-time hysteresis modeling.
- Orange County Transit Bus, California Unified, US06, and New York City Cycle are validated.

GRAPHICAL ABSTRACT

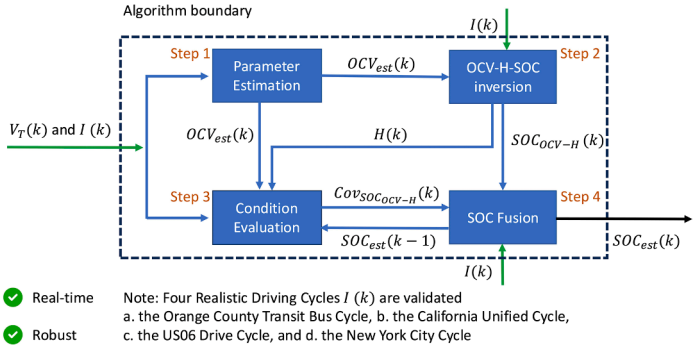

ARTICLE INFO

Keywords:
Li-ion batteries
SOC estimation
Battery management system
Adaptive control
Robust estimation

ABSTRACT

Accurate and robust state-of-charge (SOC) estimation remains a critical challenge for lithium iron phosphate (LFP) batteries due to their flat SOC–open-circuit-voltage (OCV) characteristics, pronounced hysteresis, and non-ideal operating conditions such as current sensor bias, voltage quantization, temperature variation, and insufficient excitation. This paper proposes an adaptive SOC estimation framework that addresses these challenges through an information-aware fusion strategy. The method adaptively fuses Coulomb counting and voltage-based SOC estimation using Fisher information, allowing the estimator to automatically adjust its reliance on each source according to excitation conditions and SOC–OCV observability. To explicitly capture hysteresis effects, a three-dimensional OCV–hysteresis–SOC (OCV–H–SOC) mapping is introduced for reliable SOC inversion within extended flat voltage plateaus. The proposed method is experimentally validated on an LFP cell using four realistic driving cycles under a wide range of challenging scenarios, including large initial SOC errors, prolonged operation in SOC–OCV flat zones, current bias, voltage quantization noise, low-temperature operation (10 °C), and insufficient current excitation. Compared with state-of-the-art benchmarks, including the unscented Kalman filter (UKF), LSTM, and Transformer-based estimators, the proposed approach consistently achieves superior accuracy and robustness across all tested conditions. In particular, the proposed method reduces SOC estimation error by up to approximately 80% relative to the UKF, while maintaining real-time computational efficiency.

* Corresponding author.
E-mail address: shengyu.tao@chalmers.se (S. Tao).

https://doi.org/10.1016/j.egyai.2026.100693

Available online 11 February 2026

1. Introduction

1.1. Background and motivation

Lithium Iron Phosphate (LFP) batteries stand out for their safety, long cycle life, and cost-effectiveness in applications such as electric vehicles (EVs) and energy storage systems. The accuracy of State of Charge (SOC) estimation directly impacts operational efficiency by preventing overcharging or deep discharging, thereby enhancing battery life and safety [1]. It facilitates precise energy management in EVs and storage systems [2], allowing for optimized energy allocation [3]. Moreover, reliable SOC estimation improves user confidence in EVs by providing accurate range and charging time predictions [4] and optimal route planning [5]. These needs necessitate advanced, high accuracy SOC estimation techniques for LFP cells that can adapt to diverse operating conditions.

However, SOC estimation for LFP batteries presents unique challenges due to their flat SOC—Open Circuit Voltage (OCV) curve [6]. This flat SOC—OCV plateau weakens observability by mapping measured voltage signals to SOC value to estimate. Additionally, hysteresis effects in LFP cells significantly influence OCV variations, which can be more than SOC changes themselves. In real-world applications, non-ideal conditions such as operation in SOC—OCV flat zones, current bias, voltage quantization errors, and temperature variations further complex the SOC estimation challenge in the presence of hysteresis effects [7]. Thus, a reliable, efficient, and flexible hysteresis effects modeling techniques for LFP batteries are urgently needed.

1.2. Literature review

Accurate SOC estimation is crucial for the effective LFP battery management. The most basic method is Coulomb counting, often employed due to its simplicity. However, as an open-loop method, Coulomb counting suffers from two significant drawbacks: (1) the inability to correct for initial SOC errors and (2) the accumulation of errors due to current bias and capacity estimation inaccuracies [8].

To address these issues, various advanced methods have been developed. Physics-based methods utilize mathematical models to describe the electrochemical processes and dynamic behavior of batteries [9]. The motivation for using model-based methods lies in their ability to provide a physically interpretable framework that accurately represents the internal states and dynamics of the battery [10]. These methods employ equivalent circuit models (ECM) or more complex electrochemical models, combining Coulomb counting and the inverse of the cell's OCV to get a more accurate SOC estimation [11]. The most popular model-based methods include the extended Kalman filter (EKF) [12] and unscented Kalman filter (UKF) [13]. The EKF is widely used due to its ability to handle non-linear dynamics and recognize model and measurement uncertainties [14]. In [15], an EKF observer is developed for Li-ion battery SOC and State-of-Health (SOH) estimation. However, the EKF suffers from linear approximation issues that compromises battery dynamic behaviors. The UKF addresses linearity limitations by using a deterministic sampling approach to capture mean and covariance estimates more accurately. A UKF applied to a reduced-order model for highly non-linear lithium-ion concentration and SOC estimation is presented in [16]. Literature [17] proposes a PSO-optimized ASRCKF framework for SOC estimation that systematically tunes the moving estimation window, reducing manual trial-and-error and significantly improving estimation accuracy and robustness across different temperatures, drive cycles, and initial SOCs. However, these gains come at the cost of increased computational complexity and reliance on offline metaheuristic optimization. The performance of these model-based methods is highly sensitive to the model parameters. As these parameters become less accurate with battery aging, temperature changes, and current variations, the performance of these methods deteriorates. Additionally, these methods typically model the measurement covariance matrix and process noise covariance matrix as constant hyperparameters, so the fusion of the Coulomb counting and the inverse of the OCV function is usually suboptimal and biased [15,18].

Data-driven methods leverage machine learning and statistical analysis methodologies to predict SOC based on historical data and observed patterns [19,20]. The motivation of applying data-driven methods stems from their ability to model complex, non-linear relationships without requiring detailed first principles models [21]. The typical data-driven methods include deep neural networks (DNN), long short-term memory (LSTM) networks, and transformer models [22]. DNNs are capable of modeling complex, non-linear relationships between battery measurement data and SOC [23]. Since battery measurement data are time-series data, LSTM networks, a type of recurrent neural network (RNN), are suitable to capture long-term temporal dependencies in battery behavior. An LSTM-based approach for SOC estimation is developed in [24], showing a fast convergence speed to the true SOC with sequential current, voltage, and temperature measurement data as the inputs. To focus more on the entire input sequence and address the vanishing gradient problem, transformer models with attention mechanisms have been adapted in the battery state estimation field. A transformer model for SOC estimation was investigated in [25] with a 64-second sliding window size, yielding better results than the LSTM method. In addition, [26] proposed a dynamic neural network combined with a Sage_Husa adaptive Kalman filter for LFP SOC estimation, showing improved performance compared to traditional filters. Despite their superior in capturing highly non-linear measurement-target pairs, interpretability remains a significant bottleneck [27]. More importantly, data-driven model performances are obtained under designed test conditions with specific training data [28–30]. While in practical scenarios such as battery reuse and recycling, these measurement data is scarce and heterogeneous, calling for more extensive data curation or more advances learning techniques such as collaborative and generative machine learning [31–34].

Compared to well-studied NMC cells [35], accurate SOC estimation for LFP batteries remains more challenging due to their flat OCV characteristics and inappropriate hysteresis effects modeling. For instance, [26] proposes a NARX dynamical neural network to address the flat SOC—OCV curve of LFP cells but sacrifices time efficiency for accuracy [36] uses PCA-based features with an ANN for LFP SOC estimation, but it is highly data-dependent and lacks physical interpretability, limiting robustness and generalization. Similarly, [37] introduces an adaptive recursive square root algorithm for real-time OCV and parameter identification but overlooks hysteresis and operational condition impacts. Due to the flat OCV-SOC curve, the effect of hysteresis on OCV variations can be more significant than the SOC, thus neglecting hysteresis in LFP cell SOC estimation can lead to considerable errors. While Jöst et al. [38] demonstrate robust UKF performance under frequency containment reserve conditions, hysteresis-induced voltage ambiguities and current measurement errors degrade the estimation accuracy with dynamic load shifts. Weak SOC—OCV observability further exacerbates vulnerability to sensor biases, particularly when LFP cells operate in their flat OCV range for extended periods. Shi et al. [8] combine online parameter estimation with DNN to mitigate current bias but struggle under constant-current conditions due to insufficient excitation persistence. These efforts underscore unresolved challenges: (1) balancing robustness with computational efficiency, (2) ensuring adaptability to varying operational conditions, and (3) addressing the intertwined effects of flat SOC—OCV, hysteresis, and sensor bias.

In summary, current battery SOC estimation methods face several significant limitations. The mainstream approaches lack the adaptability needed to account for changes in battery characteristics, such as hysteresis effect, over time. While online parameter estimation methods offer the potential to update parameters [39], they perform poorly when persistency of excitation conditions are not satisfied due to the flatness of OCV-SOC relationship, and the hysteresis effect that further complicates this relationship.

To the best of the authors' knowledge, existing SOC estimation methods do not provide an integrated mechanism that explicitly exploits information gain induced by dynamic current excitation to adaptively fuse multiple SOC estimation sources. In particular, the fusion between Coulomb counting and parameter-identification-based SOC estimation is typically performed using fixed or heuristically tuned weighting strategies, without accounting for time-varying excitation richness or SOC–OCV observability. This limitation is especially problematic for LFP batteries, where prolonged operation in flat OCV–SOC regions and the presence of current measurement bias severely degrade voltage-based correction capability. As a result, conventional fusion or filtering approaches may yield biased or slowly converging SOC estimates under realistic operating conditions. The present work directly addresses this gap by introducing an information-aware SOC fusion framework that adaptively adjusts estimation reliance based on Fisher information, thereby improving SOC accuracy and robustness in both electric vehicle and grid energy storage applications.

1.3. Contribution

To address the above challenges, this paper proposes an adaptive SOC estimation framework for LFP batteries that integrates real-time parameter estimation, hysteresis-aware SOC inversion, and information-based condition evaluation. The method combines Coulomb counting and voltage-based SOC estimation through a Fisher-information-guided fusion strategy, enabling automatic adaptation to variations in current excitation and SOC–OCV observability. A three-dimensional OCV–hysteresis–SOC mapping is introduced to explicitly account for hysteresis effects during SOC inversion, allowing reliable estimation within extended flat voltage regions. The proposed framework is designed for real-time implementation and is experimentally validated under diverse and challenging operating conditions, demonstrating superior robustness and accuracy compared with state-of-the-art model-based and data-driven approaches."

The key contributions of this study include:

- The novel SOC fusion strategy was proposed for adaptively combining Coulomb counting and parameter-identification based method using the information gain resulted from the dynamic cycling profiles.
- The first 3D map that captures the relationship between OCV, hysteresis, and SOC was proposed as the backbone of widely adopted parameter-identification based method, which now lacks of the critical hysteresis effect information.
- The proposed SOC estimation algorithm is mathematically provable that the estimation performance is irrelevant to current measurement bias, which can be regarded as the most significant error source of existing methods.

1.4. Organization of the paper

The organization of this paper is as follows. Section II introduces the methodologies and the four different modules employed in this study. Section III presents the test results and provides an analysis of these results under various operational conditions. Lastly, Section IV encapsulates the key conclusions drawn from this study.

2. Methodology

This section provides an overview of the system. It clarifies the role and functionality of each module within our proposed framework for SOC estimation in LFP batteries. Following this overview, we delve into the specific methodologies of each module in the subsequent subsections.

2.1. System overview

Fig. 1 presents a schematic representation of the proposed system's architecture and flow. The system is structured into four distinct but interconnected modules, each contributing a vital element to the overall SOC estimation process. The model parameter structure can be found in the Table 1. A brief summary of each module is as follows:

1. **Parameter Estimation Module (PEM):** This module forms the foundation of our system and enables adaptation to battery aging. It takes terminal voltage and current as inputs to estimate parameters, particularly the OCV. The battery dynamics are transformed into a linear format, which decouples the impact of current bias on OCV estimation. The specifics of the Parameter Estimation Module are elaborated in Section II.B.
2. **OCV-H-SOC Inversion Module (OIM):** Utilizing the OCV (OCV_{Est}) estimated by the Parameter Estimation Module, the OCV-H-SOC Inversion Module computes the hysteresis factor and determines the SOC (SOC_{OCV-H}) based on the intrinsic OCV-H-SOC map of LFP cells. A more detailed description of this module is provided in Section II.C.
3. **Condition Evaluation Module (CEM):** To ensure the reliability of SOC estimations, the Condition Evaluation Module adaptively quantifies the covariance ($cov_{SOC_{OCV-H}}$), which ascertains the confidence levels of SOC_{OCV-H} using Fisher information and the LFP cell OCV-SOC relationship. The intricacies of the evaluation process are detailed in Section II.D.
4. **SOC Fusion Module (SFM):** The final stage of the estimation system is the SOC Fusion Module. This module takes $cov_{SOC_{OCV-H}}$ and SOC_{OCV-H} as inputs and fuses them with the Coulomb counting method through a Kalman filter. This module smooths out potential noise and corrects for biases. The operational framework and benefits of the SOC Fusion Module are further discussed in Section II.E.

2.2. Parameter estimation module

The objective of the parameter estimation module is to estimate the battery parameters, particularly the OCV, in real time. To achieve this, we formulate a linear-in-the-parameters model, which facilitates the application of conventional parameter identification techniques, including the Kalman filter [40], recursive least squares, and linear regression [41].

Despite the availability of higher-order equivalent circuit models, first- and second-order Resistance-Capacitance (1RC and 2RC) models remain the predominant choice for online parameter identification and state estimation in battery management systems due to their favorable balance between model fidelity, identifiability, and real-time implement ability. Recent studies continue to adopt 1RC or 2RC structures for SOC and SOH estimation, particularly in applications requiring online adaptation and embedded implementation [42].

As shown in Fig. 2, the battery dynamics can be presented as a 2RC ECM with the following equations,

$$\dot{V}_1(t) = -\frac{1}{R_1 C_1} V_1(t) + \frac{I(t)}{C_1} \tag{1}$$

$$\dot{V}_2(t) = -\frac{1}{R_2 C_2} V_2(t) + \frac{I(t)}{C_2} \tag{2}$$

$$V_T(t) = OCV - R_0 I(t) - V_1(t) - V_2(t) \tag{3}$$

The ECM consists of an OCV, an ohmic resistor (R_0), and two RC pairs, denoted as (R_1 and C_1) and (R_2 and C_2). The current flowing through the ECM is represented by I (in Amperes), while V_1 and V_2 indicate the voltages across the two RC pairs, respectively. The terminal voltage (V_T) serves as the output of the ECM.

By assuming that values of OCV, R_0, C_1 and C_2 remain constant

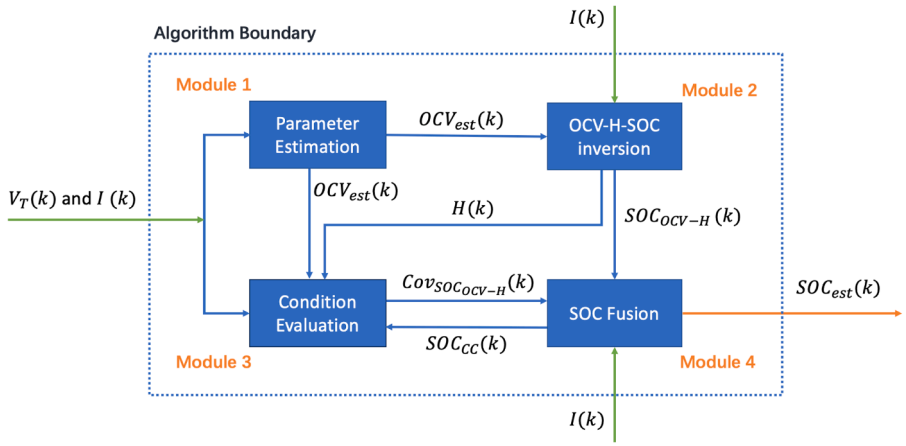

Fig. 1. Frame and flow chart of the proposed system.

Table 1
The model parameter structure.

Module	Inputs	Outputs	Parameters
PEM	V_T, I	OCV_{est}	λ_0, λ_1, N
OIM	OCV_{est}, I	H, SOC_{OCV-H}	C, f_{SOC}
CEM	$V_T, I, H, OCV_{est}, SOC_{CC}$	Cov_{OCV-H}	$\sigma_{V_T}, f_{\frac{dSOC}{dOCV}}, N$
SFM	$SOC_{OCV-H}, Cov_{OCV-H}, I$	SOC_{est}	$C_P, \Delta t, v_I$

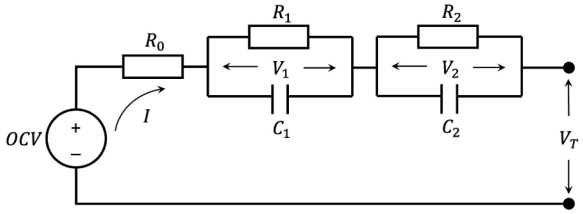

Fig. 2. Second-order ECM for battery.

during each parameter estimation step, we can apply the Laplace transform to the aforementioned equations, yielding the following equation after some substitution,

$$\begin{aligned} V_T(s) = OCV &- \tau_1\tau_2 R_0 s^2 I(s) - (R_0\tau_1 + R_0\tau_2 + R_1\tau_2 + R_2\tau_1)sI(s) \\ &- (R_0 + R_1 + R_2)I(s) - \tau_1\tau_2 s^2 V_T(s) - (\tau_1 + \tau_2)sV_T(s) \end{aligned} \tag{4}$$

where s is the complex Laplace variable, and τ_1 and τ_2 represent the time constants of the two RC pairs, calculated as R_1C_1 and R_2C_2 respectively. We can then rearrange the equation into the following form,

$$V_T = [\,OCV \quad a \quad b \quad c \quad d \quad e\,] \begin{bmatrix} 1 \\ -\ddot{I} - \dot{I} - I - \ddot{V_T} - \dot{V_T} \end{bmatrix} \tag{5}$$

where the parameters a, b, c, d, and e are defined as follows:

$$\begin{cases} a = \tau_1\tau_2 R_0 \\ b = R_0\tau_1 + R_0\tau_2 + R_1\tau_2 + R_2\tau_1 \\ c = R_0 + R_1 + R_2 \\ d = \tau_1\tau_2 \\ e = \tau_1 + \tau_2 \end{cases} \tag{6}$$

In this representation, the battery dynamics are transformed into a linear format. The detailed derivation of the linear-in-parameter formulation is provided in Appendix V.A. By utilizing the measured terminal voltage V_T, its first and second derivatives $\dot{V_T}$ and $\ddot{V_T}$, along with the current I and its derivatives $\dot{I}$ and $\ddot{I}$, we can estimate the parameters OCV, a, b, c, d, and e. It is worth noting that our method identifies OCV and the grouped coefficients (a, b, c, d, e) in the linear-in-parameter model, rather than individual RC parameters. In the linear format, the OCV is not directly related to the current (I). This implies that if there is a current bias, the term c, which represents the sum of the resistances of the battery, would absorb its impact. This property is critical, as it enables our SOC estimation scheme to be robust to current measurement bias.

In practical scenarios, the requirement for derivatives of measured signals presents a challenge due to measurement noise. To address this, we apply a second-order filter with stable poles (by setting $\lambda_0, \lambda_1 > 0$) to the measured signals. This filter design smooths out high-frequency noise while preserving the essential dynamic behavior of the LFP cell. Thus, the poles of the filter are chosen to be faster than the dynamics of the battery parameters. Typically, the time constants of the filter are an order of magnitude smaller than the time constants of battery (on the order of seconds to minutes) [43]. The second-order filter is defined as,

$$\Lambda(s) = \frac{\lambda_0}{s^2 + \lambda_1 s + \lambda_0} \tag{7}$$

Then, we have,

$$V_T\Lambda(s) = [\,OCV \quad a \quad b \quad c \quad d \quad e\,] \begin{bmatrix} 1 \\ -\ddot{I} - \dot{I} - I - \ddot{V_T} - \dot{V_T} \end{bmatrix} \Lambda(s) \tag{8}$$

$$V_T\mathrm{G}_0(s) = [\,OCV \quad a \quad b \quad c \quad d \quad e\,] \begin{bmatrix} 1 \\ -I\mathrm{G}_2(s) \\ -I\mathrm{G}_1(s) \\ -I\mathrm{G}_0(s) \\ -V_T\mathrm{G}_2(s) \\ -V_T\mathrm{G}_1(s) \end{bmatrix} \tag{9}$$

$$\begin{cases} \mathrm{G}_0(s) = \dfrac{\lambda_0}{s^2 + \lambda_1 s + \lambda_0} \\ \mathrm{G}_1(s) = \dfrac{\lambda_0 s}{s^2 + \lambda_1 s + \lambda_0} \\ \mathrm{G}_2(s) = \dfrac{\lambda_0 s^2}{s^2 + \lambda_1 s + \lambda_0} \end{cases} \tag{10}$$

where $\mathrm{G}_0(s)$, $\mathrm{G}_1(s)$, and $\mathrm{G}_2(s)$ are three transfer functions which can be

further discretized using zero-order hold and applied to the measurement signals, V_T and I. The discretized transfer functions can be represented as $G_0(z)$, $G_1(z)$, and $G_2(z)$ in the z-domain. The filtered and discretized measurement signals are then used for the paramter identification as follows,

$$\widehat{V}_T[k] = [\,OCV \quad a \quad b \quad c \quad d \quad e\,] \begin{bmatrix} 1 \\ -\widehat{I}''[k] \\ -\widehat{I}'[k] \\ -\widehat{I}[k] \\ -\widehat{V}_T''[k] \\ -\widehat{V}_T'[k] \end{bmatrix} \tag{11}$$

where $\widehat{V}_T[k]$, $\widehat{V}_T'[k]$, and $\widehat{V}_T''[k]$ are the filtered and discretized terminal voltage and its first and second derivatives, and $\widehat{I}[k]$, $\widehat{I}'[k]$, and $\widehat{I}''[k]$ are the filtered and discretized current and its first and second derivatives at the time step k. The detailed derivation of the filtered and discretized signal derivatives used for real-time implementation is provided in Appendix V.B.

Utilizing filtered and discretized signals as inputs, along with the derived linearized battery model, enables real-time estimation of battery OCV (denoted as OCV_{est}) using standard parameter identification techniques such as the KF and Recursive Least Squares (RLS) with forgetting factors. In terms of battery dynamics, SOC reflects the long-term energy state of the system, changing more gradually than voltage or current, which can fluctuate rapidly. For most users, SOC estimation does not require millisecond- or even second-level updates, only an accurate, stable indication of available energy is needed. Furthermore, high-frequency updates using noisy signals may degrade accuracy by amplifying measurement noise.

Therefore, in this study, we adopt a batch least-squares estimation approach using a 100-second moving window. While recursive techniques like RLS and KF are fully compatible with our framework, we chose the moving window approach due to its practical simplicity and tighter integration with the overall system structure. First, it reduces implementation complexity, requiring only the window length as a tuning parameter, unlike RLS or KF, which need tuning of initial covariances, process and measurement noise models, and forgetting factors. Second, the moving window structure maintains consistency with the Condition Evaluation Module (Section II.D), which computes the Fisher Information Matrix over the same time window to evaluate parameter observability and SOC estimation confidence. Switching to RLS or KF would require fundamental redesign of this calculation, such as implementing weighted sensitivity matrices or incorporating time-varying decay.

The 100-second window size was selected after a sensitivity study balancing stability, responsiveness, and computational cost. Shorter windows were more responsive but prone to noise, while longer ones offered stability at the cost of delay. A 100-second horizon (100 samples at 1 Hz) offered the best trade-off across all tested scenarios, enabling accurate, stable, and robust parameter estimates.

2.3. OCV-H-SOC inversion module

As shown by the experimental data in Fig. 3, there a significant hysteresis between the charging and discharging OCV of a LFP battery cell. This section presents the module for estimating the SOC of LFP cells, incorporating the relationship between OCV, hysteresis, and SOC. This module is referred to as the "OCV-H-SOC Inversion Module" because it inverts the relationship between OCV, hysteresis, and SOC to determine SOC from given OCV and hysteresis information.

In this study, the OCV is defined following the standard convention in battery research as the equilibrium potential of the cell under zero-current conditions after sufficient rest time to allow full electrochemical relaxation. Because extended rest periods are often impractical in experimental characterization, the quasi-equilibrium OCV is commonly approximated by applying a very low C-rate to minimize polarization losses [44].

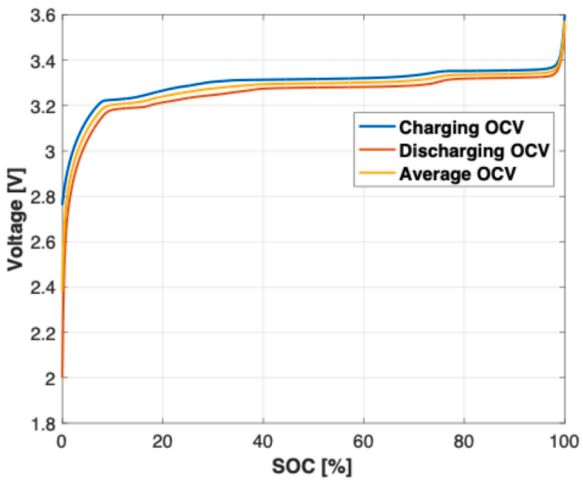

Fig. 3. LFP cell SOC–OCV curves obtained using charge and discharge at 1/50 C-rate and 25 °C for a LithiumWerks APR18650M1-B cell (3.3 V, 1.2 Ah). The "average OCV" curve shown here is defined as the mean of the charging and discharging OCV values at each SOC point.

Accordingly, the SOC–OCV relationship of the LithiumWerks APR18650M1-B cell was characterized at 25 °C using galvanostatic charge and discharge at a 1/50 C-rate. Due to the intrinsic hysteresis behavior of LFP chemistry, distinct voltage trajectories are observed during charge and discharge even at identical SOC values, resulting in voltage memory effects that cannot be captured by a single-valued SOC–OCV curve.

To explicitly characterize and validate these hysteresis effects, the cell was cycled under a sequence of partial charge–discharge loops with progressively shifted SOC limits, ensuring that the same SOC points are revisited under different charge–discharge histories (see Fig. 4). This experimental protocol systematically exposes voltage hysteresis under quasi-equilibrium conditions. The resulting charge and discharge OCV characteristics were subsequently employed to construct the hysteresis-aware OCV–H–SOC map (Fig. 6 and Fig. 7).

The hysteresis observed in LFP cells during charging and discharging can be primarily attributed to the movement of phase boundaries between Li-rich ($LiFePO_4$) and Li-poor ($FePO_4$) phases [45,46]. This phase

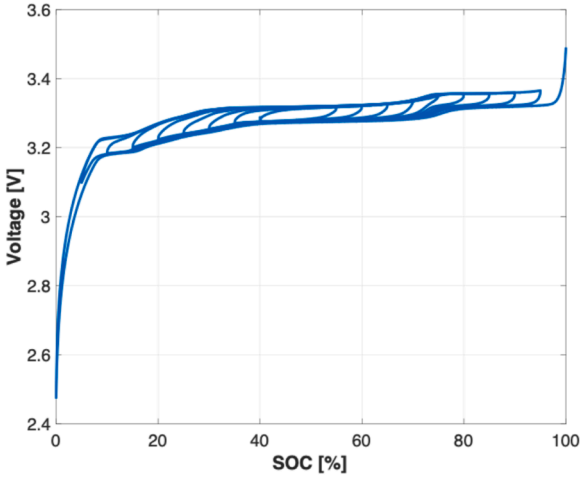

Fig. 4. Experimental characterization of voltage hysteresis in an LFP cell.

transition behavior, driven by intercalation and deintercalation processes, causes asymmetrical voltage responses during charge and discharge cycles, leading to observable hysteresis in the OCV [47,48]. This transition introduces energy barriers that result in a path-dependent voltage response, which must be captured for accurate SOC estimation.

To account for this, we adopt a recursive hysteresis model [49]. This model have been extensively validated both analytically and experimentally in the literature [50–52]. However, to improve integration within our real-time SOC estimation framework, we simplify the model by removing the explicit hysteresis voltage term and instead introducing a hysteresis factor, H, that captures the memory and directionality of phase boundary motion. This hysteresis factor is dynamically updated as:

$$H(k) = \exp\left(-\left|\frac{I(k-1)}{C}\right|\right)H(k-1) + \left(1-\exp\left(-\left|\frac{I(k-1)}{C}\right|\right)\right)sign(-I(k-1)) \tag{12}$$

Here, $I(k-1)$ is the current at the previous time step, C is a fitting parameter that determines how responsive the hysteresis state is to current magnitude, and the sign$(-I(k-1))$ term indicates the direction of the current (positive for discharging, negative for charging). The model uses an exponential term to weight the previous hysteresis state by a factor that decays with an increasing magnitude of current, thus providing a memory-like effect that captures the inertia in phase boundary movements. The sign function adjusts whether the hysteresis increases or decreases, depending on whether the cell is being charged or discharged. The model also captures how quickly the battery responds to changes in operational conditions, with a faster response at higher currents due to reduced exponential weighting. This formulation mimics the underlying phase boundary dynamics and allows the SOC—OCV-H mapping to reflect the true battery behavior across transitions.

This simplified recursive model is particularly suitable for SOC estimation in LFP cells, where the dominant hysteresis behavior arises from phase transition dynamics. By representing hysteresis through the factor H, it captures the essential path-dependent voltage response while remaining computationally efficient and implementable in real-time battery management systems. The hysteresis factor ranges between −1 and 1, corresponding to fully discharging- and fully charging-dominated phases, respectively. This approach offers a computationally efficient and physically meaningful way to incorporate hysteresis into our estimation system. The associated phase transition dynamics between Li-rich and Li-poor regions that give rise to this behavior are illustrated in Fig. 5. In real-world BMS implementations, the hysteresis factor H is continuously updated even during parking conditions, as the BMS typically remains operational. The initial value of H is set using the final value from the previous cycle. If unavailable, the low-pass filter nature of the update equation ensures fast convergence once the system resumes operation.

As shown in Fig. 6, determining SOC from an estimated OCV value depends on the hysteresis factor, H. For instance, with $H = 1$, indicating a charging-dominated case, an OCV of 3.3 V corresponds to a SOC of 28.22 %. Conversely, for $H = -1$, reflective of a discharging-dominated case, the same OCV of 3.3 V corresponds to a SOC of 74.11 %. When $H = 0$, suggesting an equilibrium state within the hysteresis loop, the SOC is 51 % for an OCV of 3.3 V. These relationships enable us to construct a 3D mapping between SOC, OCV, and the hysteresis factor using experimental data, as shown in Fig. 7.

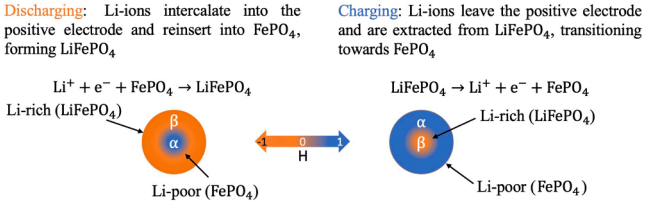

Fig. 5. Phase transition between Li-rich and Li-poor phases.

As shown in the Fig. 8, in the OCV-H-SOC inversion module, the hysteresis term H is estimated in open-loop via Eq. (12), using the current as input. Then, utilizing the estimated OCV (denoted as OCV_{est}) from the parameter estimation module, along with the hysteresis term, we employ the OCV-H-SOC relationship 3D map (Fig. 7) to determine the SOC (denoted as SOC_{OCV-H}) as follows,

$$SOC_{OCV-H}(k) = f_{SOC}(OCV_{est}(k), H(k)) \tag{13}$$

This step is implemented as a numerical interpolation in the 3D map.

2.4. Condition evaluation module

In battery state estimation, the availability and reliability of voltage-based information strongly depend on the observability of the underlying states and parameters, which in turn is governed by the richness of the input current excitation. This issue is particularly critical for LFP batteries, where the SOC–OCV relationship exhibits extended flat regions, rendering voltage measurements weakly informative over a wide SOC range. Under such conditions, blindly applying voltage-based correction or fixed fusion rules can lead to biased or overconfident SOC estimates. To address this challenge in a principled manner, a condition evaluation metric is required that can quantitatively assess the information content of the measured signals with respect to the estimated parameters and SOC. Fisher information provides a natural and theoretically grounded choice for this purpose, as it directly characterizes the sensitivity of the measurement model to unknown parameters and states, and is fundamentally linked to estimation uncertainty through the Cramér–Rao lower bound [53]. This evaluation enables us to quantify parameter uncertainty. Besides, when the estimation system operates in the SOC—OCV flat zone, roughly from 20 % to 95 % SOC, the SOC estimation uncertainty is heightened. Thus, this module quantities the covariance and confidence levels of the SOC estimated from the *OCV-H-SOC Inversion Module*.

According to Eq. (11), with the filtered and discretized terminal voltage as the measurement output, we determine the sensitivity, $S(k)$, of the voltage to each parameter by computing the partial derivatives of the output with respect to each parameter,

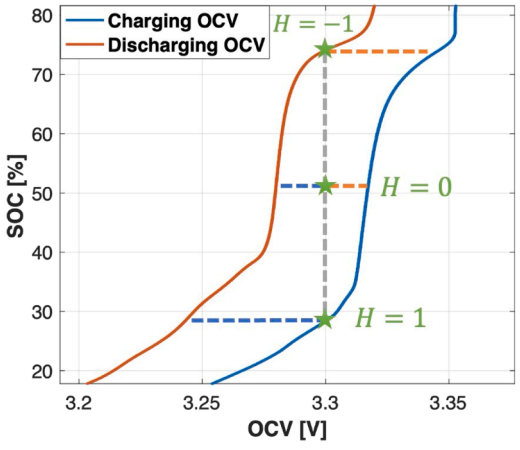

Fig. 6. Example of SOC estimation from OCV using the hysteresis factor $\boldsymbol{H}$ (Eq. (12)). The same OCV corresponds to different SOC values depending on charge ($\boldsymbol{H} = 1$), discharge ($\boldsymbol{H} = -1$), or intermediate ($\boldsymbol{H} = 0$) states.

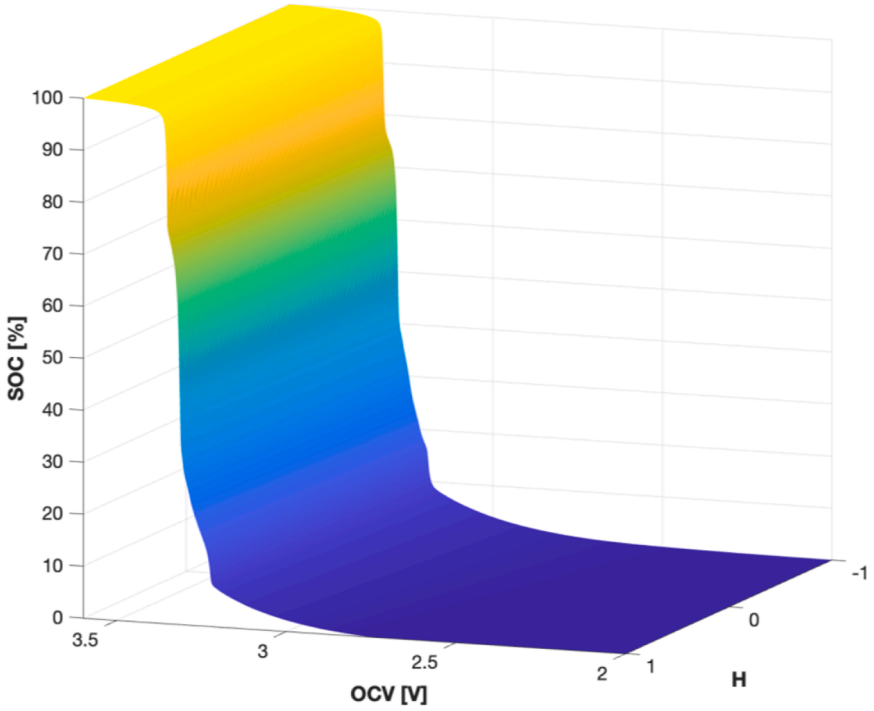

Fig. 7. OCV-H-SOC relationship 3D map, $f_{SOC}(OCV, H)$, constructed from experimental data.

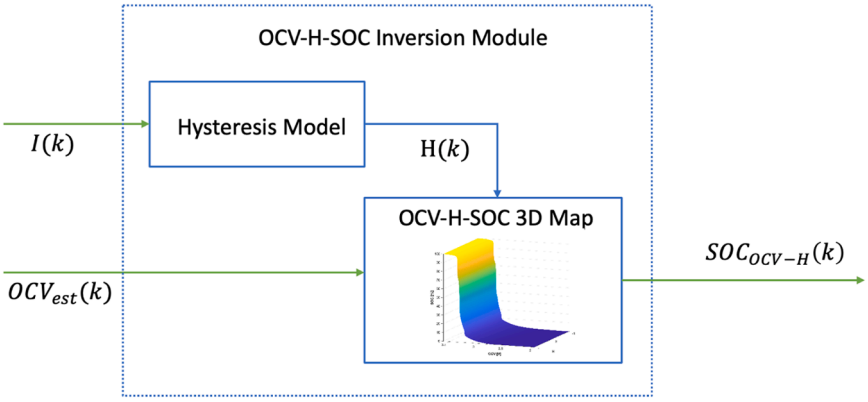

Fig. 8. The flowchart of the OCV-H-SOC Inversion Module.

$$S(k)=\begin{bmatrix} \left.\frac{\partial \widehat{V_T}}{\partial OCV}\right|_{k-N} & \left.\frac{\partial \widehat{V_T}}{\partial a}\right|_{k-N} & \left.\frac{\partial \widehat{V_T}}{\partial b}\right|_{k-N} & \left.\frac{\partial \widehat{V_T}}{\partial c}\right|_{k-N} & \left.\frac{\partial \widehat{V_T}}{\partial d}\right|_{k-N} & \left.\frac{\partial \widehat{V_T}}{\partial e}\right|_{k-N} \\ \left.\frac{\partial \widehat{V_T}}{\partial OCV}\right|_{k-N+1} & \left.\frac{\partial \widehat{V_T}}{\partial a}\right|_{k-N+1} & \left.\frac{\partial \widehat{V_T}}{\partial b}\right|_{k-N+1} & \left.\frac{\partial \widehat{V_T}}{\partial c}\right|_{k-N+1} & \left.\frac{\partial \widehat{V_T}}{\partial d}\right|_{k-N+1} & \left.\frac{\partial \widehat{V_T}}{\partial e}\right|_{k-N+1} \\ \vdots & \vdots & \vdots & \vdots & \vdots & \vdots \\ \left.\frac{\partial \widehat{V_T}}{\partial OCV}\right|_{k} & \left.\frac{\partial \widehat{V_T}}{\partial a}\right|_{k} & \left.\frac{\partial \widehat{V_T}}{\partial b}\right|_{k} & \left.\frac{\partial \widehat{V_T}}{\partial c}\right|_{k} & \left.\frac{\partial \widehat{V_T}}{\partial d}\right|_{k} & \left.\frac{\partial \widehat{V_T}}{\partial e}\right|_{k} \end{bmatrix} \tag{14}$$

Then, we have,

$$S(k)=\begin{bmatrix} 1 & -\widehat{I}''[k-N] & -\widehat{I}'[k-N] & -\widehat{I}[k-N] & -\widehat{V_T}''[k-N] & -\widehat{V_T}'[k-N] \\ 1 & -\widehat{I}''[k-N+1] & -\widehat{I}'[k-N+1] & -\widehat{I}[k-N+1] & -\widehat{V_T}''[k-N+1] & -\widehat{V_T}'[k-N+1] \\ \vdots & \vdots & \vdots & \vdots & \vdots & \vdots \\ 1 & -\widehat{I}''[k] & -\widehat{I}'[k] & -\widehat{I}[k] & -\widehat{V_T}''[k] & -\widehat{V_T}'[k] \end{bmatrix} \tag{15}$$

where $\widehat{V}_T[k]$, $\widehat{V}_T'[k]$, and $\widehat{V}_T''[k]$ are the filtered and discretized terminal voltage and its first and second derivatives, and $\widehat{I}[k]$, $\widehat{I}'[k]$, and $\widehat{I}''[k]$ are the filtered and discretized current and its first and second derivatives at the time step k, as mentioned in Section II.C. $N$is the number of data points/time steps used in the linear regression of the online parameter estimation. The Fisher information matrix, $F(k)$, is,

$$F(k)=\frac{S(k)^T S(k)}{\sigma_{V_T}^2} \tag{16}$$

Here, σ_{V_T} is the terminal voltage measurement noise covariance.

While the F(k) is ideally invertible, it may become ill-conditioned or singular under low excitation conditions. A large moving window can help alleviate this by including more informative data points. Besides, in practice, Tikhonov regularization is applied to ensure numerical stability:

$$F(k) = F(k) + \epsilon I_{d\times d} \tag{17}$$

Where $\epsilon = 10^{-8}$is a very small constant, and $I_{d \times d}$ is the $d \times d$ identity matrix matching the size F(k). This regularized matrix guarantees invertibility.

The Cramér-Rao bound provides the lower bound of the parameter estimation covariance, computed from the inverse of the Fisher information matrix [54]. Hence, we determine the lower bound of the estimated OCV's covariance by selecting the first element in the inverse Fisher information matrix,

$$Cov_{OCV} \geq \left[F(k)^{-1}\right]_{11} \tag{18}$$

Considering the nearly monotonic OCV-SOC relationship depicted in Fig. 7, and assuming no uncertainty related to the hysteresis factor, we can approximate the covariance of the estimated SOC from OCV as,

$$Cov_{SOC} = \left(\frac{dSOC}{dOCV}\right)^2 Cov_{OCV} \tag{19}$$

where $\frac{dSOC}{dOCV}$ is the inverse slope of the SOC—OCV curve, and is a function of H and SOC,

$$\frac{dSOC}{dOCV} = f_{\frac{dSOC}{dOCV}}(H, SOC) \tag{20}$$

This derivation is a critically important attribute of the algorithm. Namely, in flat zones of the OCV-SOC curve, uncertainty in OCV produces amplified uncertainty in the estimated SOC from the inversion process. As illustrated in Fig. 9, we can see that the value of $\frac{dSOC}{dOCV}$ is extremely high when H is close to 1 and SOC is around 85 %. This is because when charging is dominant, the SOC—OCV curve around 85 % SOC is almost purely flat ($\frac{dOCV}{dSOC} \approx 0$). Namely, the SOC ($SOC_{OCV-H}$) obtained from the OCV-H-SOC Inversion Module is not reliable in this case.

According to above equations, we can then estimate the covariance and confidence levels of SOC_{OCV-H} with the following relation,

$$Cov_{SOC_{OCV-H}}(k) \geq \left(f_{\frac{dSOC}{dOCV}}(H(k), SOC_{CC}(k))\right)^2 \left[F(k)^{-1}\right]_{11} \tag{21}$$

where $Cov_{SOC_{OCV-H}}$ is the covariance of estimated SOC_{OCV-H}, and $SOC_{CC}(k)$ is the estimated SOC by Coulomb counting from the SOC Fusion Module at the given time step. We assume that $SOC_{CC}(k)$ is sufficiently close to the true SOC to accurately determine $f_{\frac{dSOC}{dOCV}}$.

Based on Fig. 9 and Eq. (19), we expect that the covariance of estimated SOC from OCV-H-SOC Inversion Module ($Cov_{SOC_{OCV-H}}$) is high when the battery is in the SOC—OCV flat zone, where the value of $f_{\frac{dSOC}{dOCV}}$ is substantially high. Additionally, when the current excitation level is low, then the first element of the Fisher information matrix $\left[F(k)^{-1}\right]_{11}$ is high, which increases the covariance.

In summary, as shown in Fig. 10, the Condition Evaluation Module assesses the estimated SOC covariance from OCV-H-SOC Inversion Module under varying operational conditions.

2.5. SOC fusion module

The SOC Fusion Module serves as the integrative core of our system. It combines the traditional Coulomb counting with the estimated SOC from the *OCV-H-SOC Inversion Module*, via a Kalman filter framework. The module enhances SOC accuracy by performing the following update cycle:

Model Prediction:

Coulomb counting is utilized for real-time SOC prediction by integrating current flow over time:

$$SOC_{cc}(k) = SOC_{est}(k-1) + \frac{I(k-1)\Delta t}{C_P} \tag{22}$$

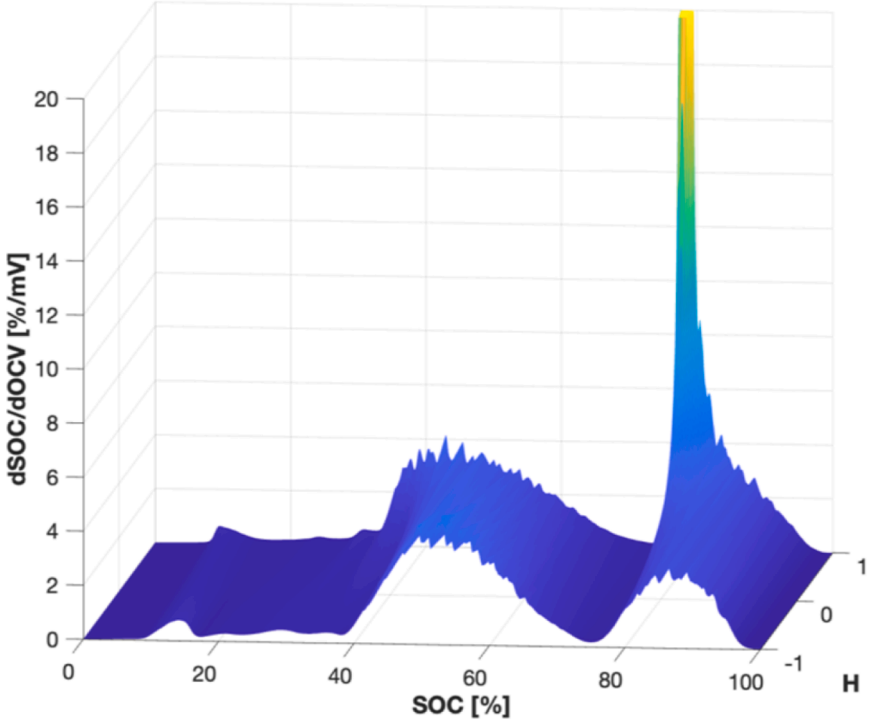

Fig. 9. The inversion of the slope of the SOC—OCV curve with the given estimated H and SOC.

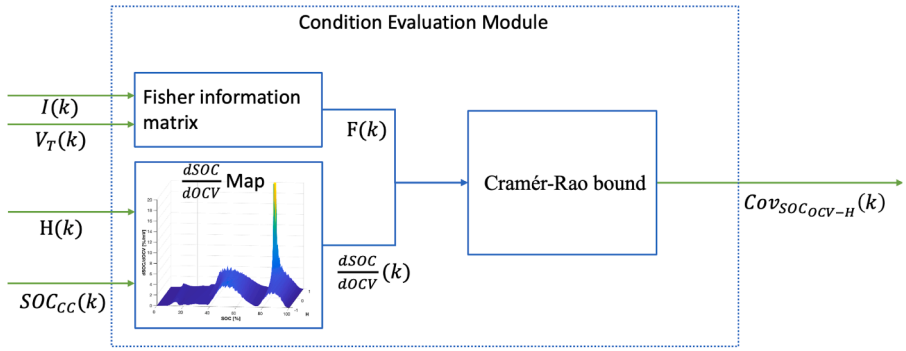

Fig. 10. The flowchart of the Condition Evaluation Module.

where $SOC_{cc}(k)$ is the SOC estimated by Coulomb counting, $I(k-1)$ is the current at the previous step, Δt is the sampling time, and C_P is the battery capacity, which is assumed to be known in advance.

Measurement update:

The SOC estimation from the OCV and hysteresis model, $SOC_{OCV-H}(k)$, is used as the measurement part of the Kalman filter.

Error Covariance Prediction:

$$P_p(k) = P_m(k-1) + v_I \tag{23}$$

The predicted error covariance, $P_p(k)$, accounts for process noise, and v_I captures uncertainties in the model prediction phase. It corresponds to the uncertainty in current measurement.

Kalman Gain Calculation:

$$K(k) = \frac{P_p(k)}{P_p(k) + cov_{SOC_{OCV-H}}(k)} \tag{24}$$

The Kalman gain, $K(k)$, determines the weighting of the measurement update relative to the predicted state, influenced by the confidence in the SOC_{OCV-H} estimates provided by the Condition Evaluation Module.

State Update:

$$SOC_{est}(k) = SOC_{cc}(k) + K(k)(SOC_{OCV-H}(k) - SOC_{cc}(k)) \tag{25}$$

The state update refines the SOC estimate, $SOC_{est}(k)$, by reconciling the differences between the Coulomb counting (model prediction) and the $SOC_{OCV-H}(k)$ (measurement correction).

Covariance Update:

$$P_m(k) = (I - K(k))P_p(k) \tag{26}$$

The updated measurement error covariance, $P_m(k)$, reflects the reduction in uncertainty following the measurement update.

While Coulomb counting offers a straightforward estimation technique by cumulative current integration, it is prone to drift from initial SOC inaccuracies and current measurement biases. Within the Kalman filter, however, Coulomb counting serves as the model, providing a baseline SOC trajectory. It is updated using SOC_{OCV-H}, which, despite being noisy, corrects Coulomb counting via OCV-H inversion.

The process noise of the Kalman filter is interpreted as the uncertainty of the current measurement. Meanwhile, the measurement noise, indicated by the covariance of SOC_{OCV-H}, modulates the confidence in updates according to the latest condition assessments. By blending Coulomb counting with SOC_{OCV-H} estimations, the SOC Fusion Module produces a synchronized SOC output, $SOC_{est}(k)$. Such calibration with real-time data allows the system to deliver a smooth SOC estimation, effectively correcting for current biases and initial SOC inaccuracies. In addition, because the Kalman filter does not rely on other battery parameters, it is less impacted by the aging and temperature effects compared to other methods mentioned in the literature review section.

3. Model performance

In this section, we begin by outlining the configuration of our test environment. We introduce a state-of-art benchmark method for comparison: the UKF approach. The proposed algorithm is then rigorously tested against the benchmark using driving cycle data and through a series of challenging scenarios. These scenarios mimic real-world complexities, including high initial SOC error, prolonged operation in SOC—OCV flat zones, current bias, voltage quantization error, low temperature, and insufficient current excitation. The results from these tests are discussed to provide a nuanced perspective on the robustness and accuracy of the proposed algorithm under various conditions.

3.1. Testing setup

In this study, we utilize a LithiumWerks APR18650M1-B, a 3.3 V, 1.2 Ah $LiFePO_4$ battery, for all tests. The ambient temperature around the battery cell is maintained at either 25 °C or 10 °C within an ESPEC BTL-433 environmental chamber. The battery is tested using an Arbin high-current cylindrical cell holder. Charge and discharge cycles, mimicking vehicle operations, are executed using a PEC SBT2050 cycler. For SOC accuracy comparison, the reference ('true') SOC was obtained by high-precision Coulomb counting using the laboratory cycler (PEC SBT2050). Before each test, a calibration was conducted: the SOC was initialized to 100 % after a full charge and to 0 % after a full discharge, determined by the manufacturer-specified cut-off voltages of 3.65 V and 2.0 V. This reference SOC served as the ground truth for validating the estimation methods.Table 2

All experimental data collected from the test bench are used consistently across all SOC estimation methods to ensure fair comparison. The measured current and voltage signals serve as inputs to both the proposed algorithm and the benchmark methods, while the reference SOC obtained from high-precision Coulomb counting is used as the ground truth for performance evaluation.

To comprehensively evaluate robustness under realistic and challenging operating conditions, a structured set of experimental scenarios is designed. Benchmark methods are first introduced in Section III.B. Baseline performance under ideal operating conditions is evaluated using the UDDS in Section III.C. The estimator behavior during

Table 2
Parameters of the LithiumWerks APR18650M1-B LFP Cell Used in This Study.

Parameter	Value / Description
Cell Chemistry	Lithium Iron Phosphate ($LiFePO_4$)
Manufacturer / Model	LithiumWerks APR18650M1-B
Nominal Voltage	3.3 V
Nominal Capacity	1.2 Ah
Energy	~3.96 Wh
Operating Voltage Range	2.0 – 3.65 V
Maximum Charge Voltage	3.65 V

prolonged operation within SOC–OCV flat zones is examined in Section III.D using multiple driving cycles. The impact of current measurement bias under prolonged flat-zone operation is investigated in Section III.E, followed by an assessment of voltage quantization effects due to ADC resolution limitations in Section III.F. The robustness of the proposed method under low-temperature operation (10 °C), with parameters identified at room temperature, is evaluated in Section III.G. Finally, Section III.H investigates system performance under insufficient excitation conditions, characterized by a long constant-current segment within the SOC–OCV flat zone.

3.2. Benchmark approaches

The classical KF provides optimal state estimation for linear systems with Gaussian noise. However, since battery models are inherently nonlinear, KF alone is rarely sufficient for SOC estimation. To validate the efficacy of our proposed SOC estimation system, we compare it against a well-established method, the UKF approach. The UKF was selected as the primary benchmark in this study because it is widely regarded as a state-of-the-art physics-based estimator for nonlinear battery dynamics. Compared to the EKF, the UKF avoids linearization errors through deterministic sampling, making it more accurate and robust for SOC estimation. Due to these advantages, the UKF has become one of the most frequently adopted benchmark algorithms in both academic research and industrial battery management systems.

In this study, parameters of the battery's 2RC model for the UKF are determined using the Hybrid Pulse Power Characterization (HPPC) test, which involves 1C discharge pulses at 5 % SOC intervals. All tests are conducted at a stable ambient temperature of 25 °C across various SOC levels. The SOC—OCV curve utilized in the UKF is derived from an average of the charging and discharging SOC—OCV curves, specifically obtained at 25 °C. The benchmark method is tested under identical testing conditions to those used for our proposed algorithm to ensure a fair and consistent comparative analysis.

In addition to the UKF, we include a comprehensive benchmarking study presented in Appendix V.C, where we implement and evaluate two leading data-driven models, LSTM and decoder-only Transformer model, both as standalone predictors and in combination with Coulomb Counting via a Kalman Filter. Appendix V.C details the model architectures, fusion strategies, test conditions, and computational costs. It also provides a comparative analysis across various realistic operating scenarios, highlighting the strengths and limitations of each method.

3.3. Under urban driving conditions

For the ideal condition test, the battery is cycled from 100 % SOC to 0 % SOC and then charged back to 100 % SOC using the Urban Dynamometer Driving Schedule (UDDS) driving cycle profile. We refer to these conditions as 'ideal' because the test is performed with no measurement errors, at a constant room temperature of 25 °C, and under a highly dynamic current profile where persistency of excitation conditions is satisfied.

As illustrated in Fig. 11, the blue, red, and yellow lines represent the SOC from the UKF, proposed method, and true values, respectively. For the ideal condition test, both methods work very well. The Root Mean Square Error (RMSE) results for the proposed method and the UKF are 0.49 % and 3.92 %, respectively. For both methods, the initial SOC guess was set at 50 % to introduce a 50 % initialization error. The plot shows that both SOC estimation methods quickly converge to the true SOC value. This rapid convergence is primarily due to the true initial SOC value being 100 %, which lies in the non-flat zone of the OCV-SOC curve. Additionally, a deliberately designed high initial SOC error covariance helps accelerate convergence in the presence of high initial uncertainty. However, although the UKF provides relatively good estimation results, its performance does not match that of the proposed method, which estimates battery parameters in real-time and accounts for the hysteresis phenomenon.

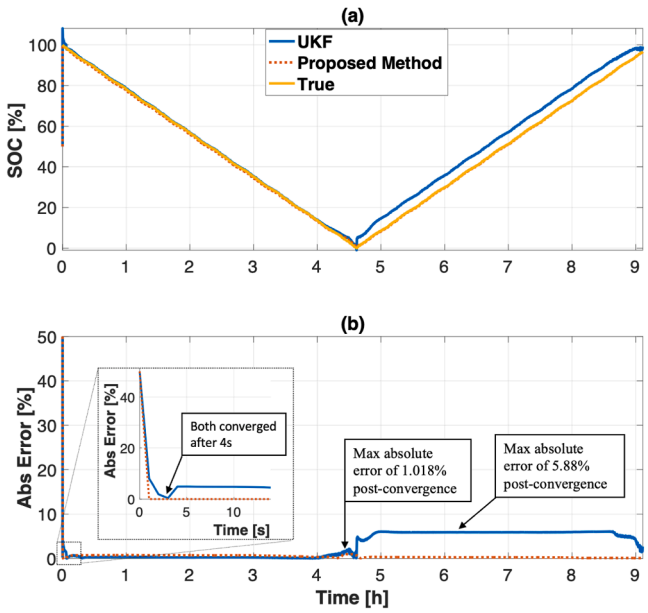

Fig. 11. Test results under ideal condition: No voltage and current measurement error, operation from 100 % to 0 % SOC at 25 °C. (a) SOC comparison between the UKF, proposed method, and true SOC. (b) Absolute error (%) comparison, showing a maximum absolute error of 1.018 % for the proposed method and 5.88 % for the UKF after convergence. The RMSE values are 0.49 % and 3.92 % for the proposed method and UKF, respectively.

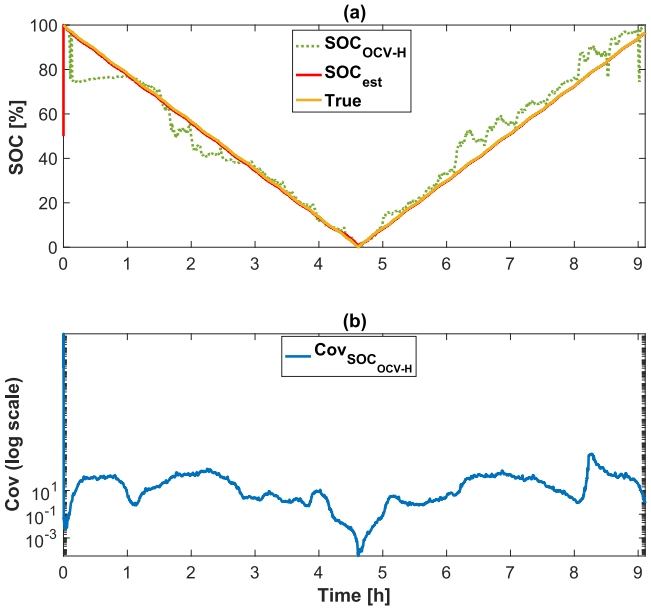

Fig. 12. Test result of the proposed method with the ideal condition. (a) SOC comparison between SOC_{OCV-H}(*SOC estimated from OCV and hysteresis model*), SOC_{est}, and true SOC. (b) Covariance of SOC from the OCV-H-SOC inversion module on a logarithmic scale.

To better illustrate the operation of the proposed method, Fig. 12 presents the SOC estimated from OCV and hysteresis SOC_{OCV-H} and its covariance $cov_{SOC_{OCV-H}}$ utilized in the SOC Fusion Module. In the subplot, it is noticeable that SOC_{OCV-H} is noisy and inaccurate, particularly between 40.5 % to 63.75 % SOC and 78.2 % to 93.15 % SOC. This inaccuracy arises because these are super flat zones in the SOC—OCV curve. As illustrated in Fig. 9, the $\frac{dSOC}{dOCV}$ values are up to 20 %/mV when SOC is around 85 % during charging, indicating that the SOC is insufficiently sensitive to variations in OCV values. Consequently, the proposed Condition Evaluation Module output notably high $cov_{SOC_{OCV-H}}$ values for the system in the super flat zones, as shown in the lower subplot of Fig. 12. Conversely, when the SOC is between 0 % to 8.75 % and 97.6 % to 100 %, the SOC—OCV curve exhibits its steepest slopes. During these intervals, the Condition Evaluation Module assigned low $cov_{SOC_{OCV-H}}$ values to the SOC Fusion Module. Thus, in this test case, the SOC Fusion Module relies more on SOC_{OCV-H} when the slope of the SOC—OCV curve is steep and leans more towards Coulomb counting when the battery operates within the SOC—OCV flat zones, ensuring the fused SOC result (SOC_{est}) greatly matches the true SOC. It performs this weighting automatically, based on the mathematical model structure and data.

3.4. Prolonged operation in soc-ocv flat zones

In this subsection, we evaluate the performance of the proposed method and the UKF specifically within the SOC—OCV flat zones, for an extended period. The battery is charged from 20 % SOC to 80 % SOC and then discharged back to 20 % SOC. Four different driving cycle profiles, including the Orange County Transit Bus Cycle (OCTBC), the California Unified Cycle (OCTBC), the US06 Drive Cycle, and the New York City Cycle (NYCC), are used to generate the current profiles for validating system performance under different operational conditions. The corresponding voltage and current profiles are shown in Fig. 13.

The test spans approximately 24 h and is exclusively conducted within the flat zone range from 20 % SOC to 80 % SOC to thoroughly assess the impact of SOC—OCV flat zones on both the proposed method and the UKF. The true initial SOC is set at 20 %, while an erroneous initial guess of 100 % SOC is intentionally set to introduce an 80 % initial error.

The comparison results are illustrated in Fig. 14. The RMSE for the proposed method and the UKF are 2.54 % and 6.69 %, respectively. The RMSE values for both methods are higher than those observed in ideal conditions, because the flat SOC—OCV zones reduce opportunities for correction that are available in steeper zones. Despite this, the proposed

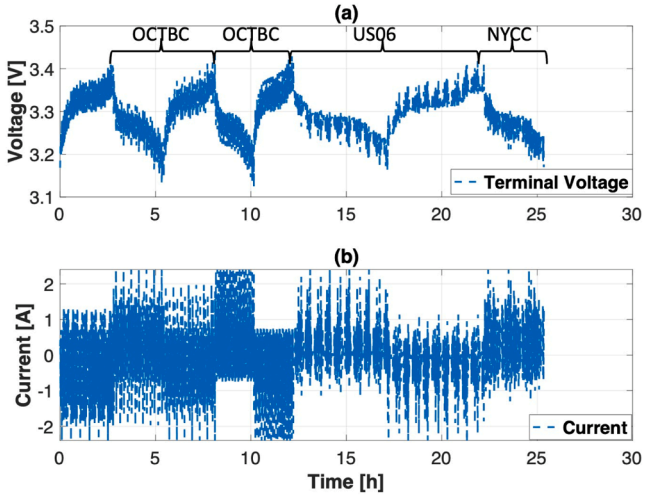

Fig. 13. Voltage and Current profiles using the Orange County Transit Bus Cycle, the California Unified Cycle, the US06 Drive Cycle, and the New York City Cycle. (a) Voltage profile. (b) Current profile.

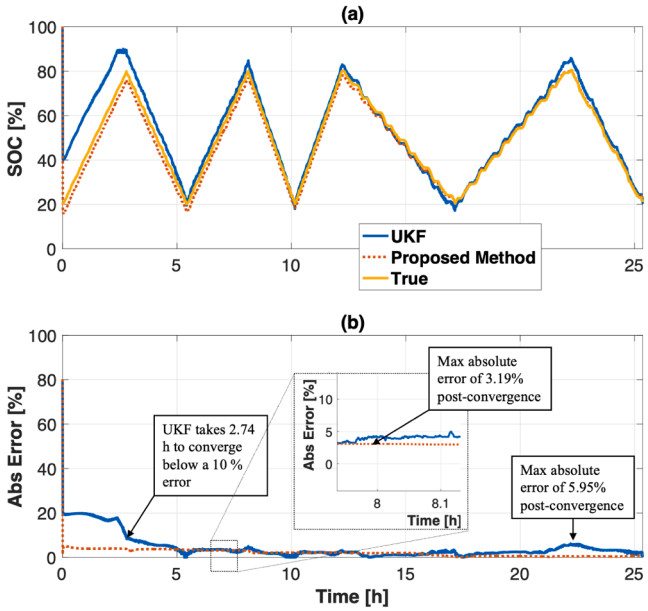

Fig. 14. Test results of the SOC—OCV flat zones (operation from 20 % to 80 % SOC at 25 °C with four different current profiles). (a) SOC comparison between the UKF, proposed method, and true SOC. (b) Absolute error (%) comparison, showing a maximum absolute error of 3.19 % for the proposed method and 5.95 % for the UKF after convergence. The RMSE values are 2.54 % and 6.69 % for the proposed method and UKF, respectively.

method still performs better than the UKF.

The state-space equations used by the UKF are:

$$\begin{bmatrix} SOC(k+1) \\ V_1(k+1) \\ V_2(k+1) \end{bmatrix} = \begin{bmatrix} 1 & 0 & 0 \\ 0 & e^{-\frac{\Delta t}{R_1 C_1}} & 0 \\ 0 & 0 & e^{-\frac{\Delta t}{R_2 C_2}} \end{bmatrix} \begin{bmatrix} SOC(k) \\ V_1(k) \\ V_2(k) \end{bmatrix} + \begin{bmatrix} -\frac{\Delta t}{C_P} \\ \left(1 - e^{-\frac{\Delta t}{R_1 C_1}}\right) R_1 \\ \left(1 - e^{-\frac{\Delta t}{R_2 C_2}}\right) R_2 \end{bmatrix} I(k) + w_{UKF} \tag{27}$$

$$V_T(k) = OCV(SOC) - I(k)R_0 - V_1(k) - V_2(k) + v_{UKF} \tag{28}$$

where R_1, R_2, C_1, and C_2 are the fitted battery RC parameters (which change crossing SOC), V_1 and V_2 are the voltages across the two RC pairs, C_P is the battery capacity, and Δt is the sampling time. V_T is the terminal voltage and R_0 is the ohmic resistance. Besides, w_{UKF} and v_{UKF} are process and measurement noises that capture model inaccuracies and measurement errors, respectively.

For the UKF, convergence to below a 10 % SOC estimation error takes 2.74 h because of its slower adjustment rate. In the flat OCV zones, reliance on predefined, nonlinear parameters makes the UKF less sensitive to OCV variations. Changes in OCV may be masked by inaccurate RC parameters or absorbed through adjustments in V_1 and V_2 with the noise terms w_{UKF} and v_{UKF}. In contrast, the proposed system is more sensitive to OCV changes. It transforms battery dynamics into a linear format, making it more responsive to OCV variations. It also updates all parameters in real time, ensuring the model quickly adapts and stays aligned with the actual battery behavior.

The corrective effort of the UKF is primarily represented by the

Kalman gain for SOC and the voltage difference between the true and predicted terminal voltages. As depicted in Fig. 10, for the UKF, the voltage error, along with the Kalman gain for SOC, drops significantly after a few iterations. The high initial SOC covariance results in a high Kalman gain at the beginning, which, combined with the high initial voltage error, leads to fast corrections initially. However, when the gain is low and the voltage difference is small due to the flat zone effect, the gain applied to the output error injection is small. Thus, the UKF essentially resembles a Coulomb counting method and converges very slowly. It is also notable that a higher process noise setup for the Coulomb counting part can help with the convergence speed. However, it also degrades the overall performance of the UKF because, within super flat zones, it must rely on Coulomb counting. Fig. 15

Conversely, as shown in Fig. 11, the SOC estimates from the proposed method converge quickly to the true SOC values, assisted by the SOC estimated from OCV-H inversion. Although the SOC_{OCV-H}values exhibit considerable noise, the SOC Fusion Module, combined with $cov_{SOC_{OCV-H}}$ from the Condition Evaluation Module, effectively mitigates the impact of the very flat SOC—OCV zone and low current excitation levels, ensuring accurate and smooth estimation results. The detailed comparison between SOC_{est}, SOC_{OCV-H}, and the true SOC is presented in the upper subplot of Fig. 11. We can see that SOC_{est} rapidly converges to the true SOC value after compensating for the initially high guess error. By cross-referencing the lower subplot of Fig. 16, the values of SOC_{OCV-H} align with the true SOC when $cov_{SOC_{OCV-H}}$ is low. Consequently, the SOC Fusion Module effectively adjusts SOC_{est} based on SOC_{OCV-H} and $cov_{SOC_{OCV-H}}$, tailored to the specific operational conditions.

3.5. Prolonged operation in soc-ocv flat zones and with current bias

Current bias is always a concern for battery state estimation, yet almost always ignored in the literature. In this subsection, the performance of the proposed method and UKF is evaluated under another extreme condition [55]. In addition to prolonged operation within the flat SOC—OCV zones with a high initial guess error, we apply a significant current bias of −0.05 A (the negative current indicates that charging here). This bias is substantial given the battery's capacity of only 1.2 Ah. Fig. 17

As illustrated in Fig. 12, the RMSE for the proposed method and the

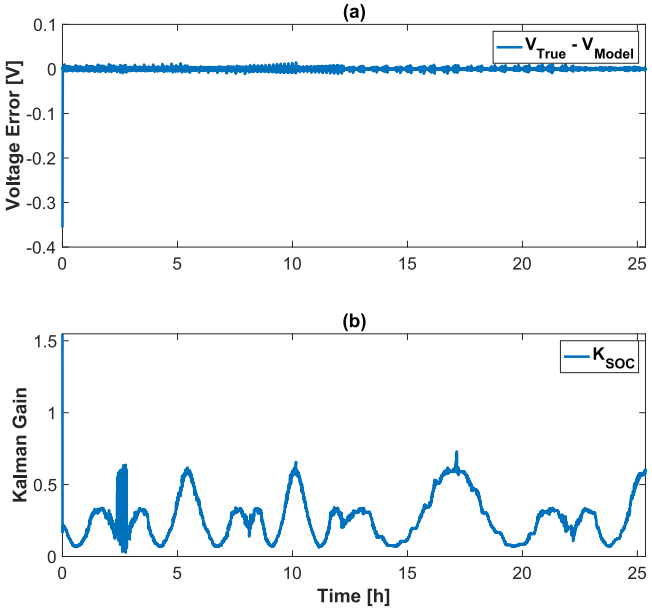

Fig. 15. Voltage prediction error and Kalman gain for the UKF method in the SOC—OCV flat zone case. (a) Error between measured and predicted terminal voltage in the UKF model. (b) Kalman gain for SOC correction in the UKF.

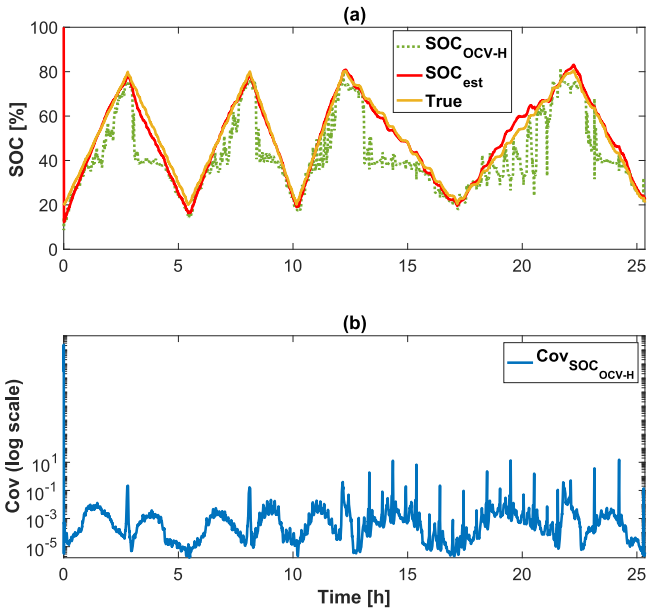

Fig. 16. Proposed method under the flat zone case. (a) SOC comparison between SOC_{OCV-H}(*SOC estimated from OCV and hysteresis model*), SOC_{est}, and true SOC. (b) Covariance of SOC from the OCV-H-SOC inversion module on a logarithmic scale.

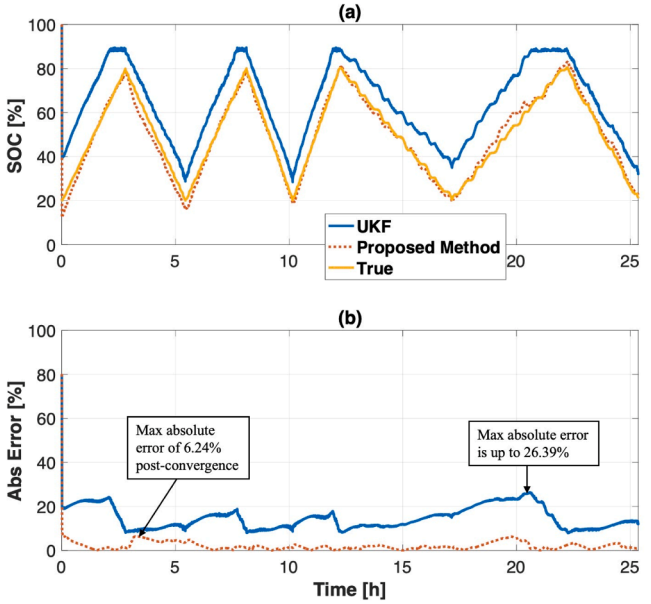

Fig. 17. Test results of the SOC—OCV flat zone adding a high current measurement bias. The operation is from 20 % to 80 % SOC at 25 °C with four different current profiles and −0.05A current bias. (a) SOC comparison between the UKF, proposed method, and true SOC. (b) Absolute error (%) comparison, showing a maximum absolute error of 6.24 % for the proposed method and 26.39 % for the UKF after convergence. The RMSE values are 2.99 % and 15.44 % for the proposed method and UKF, respectively.

UKF are 2.99 % and 15.44 %, respectively. The proposed method significantly outperforms the UKF. The UKF, being a model-based method, relies on current measurements to update the SOC, voltages across two RC pairs, and terminal voltage. Consequently, the current measurement bias adversely affects the internal state estimates and terminal voltage prediction. Suppose we set a higher process noise for the Coulomb counting part to encourage the UKF to rely more heavily on the measurement correction. This sacrifices the performance of the

method under other conditions, namely under high voltage noise, and the estimation accuracy would not significantly improve. For instance, the negative current bias increases the SOC calculated by Coulomb counting, leading to higher estimated terminal voltages and, subsequently, an overestimation of SOC. Although the UKF's internal model attempts to capture battery voltage dynamics to offset the cumulative error from Coulomb counting, the impact of current bias on internal voltages results in a significant positive SOC estimation offset of up to 26.39 % (Fig. 16).

On the other hand, the current bias has only a limited impact on the proposed method. Thanks to Eq. (8) within the Parameter Estimation Module, the current bias predominantly affects the parameter 'c', which is related to the internal resistances of the battery. The impact of current bias is absorbed by the estimation of internal resistances rather than affecting the estimated OCV. With fewer components impacted by the current bias, the proposed method maintains its performance by utilizing relatively accurately estimated OCV to mitigate accumulated SOC errors associated with Coulomb counting.

3.6. Prolonged operation in soc-ocv flat zones with voltage quantization errors

Since the SOC—OCV curve of LFP cells is quite flat, there are concerns about the impacts of voltage measurement bias and sensor noise. Voltage measurement bias refers to a systematic offset in the measured voltage, meaning that the recorded voltage values consistently deviate from the true values by a fixed amount (positive or negative). In practice, voltage measurement sensors should be periodically calibrated and updated, thus the voltage measurement bias is not modeled here. Instead, we consider voltage sensor noise, i.e., ADC (analog to digital converter) Quantization Noise as a major error source. In this subsection, voltage quantization errors were introduced to the voltage measurement results to simulate the effects of a 10-bit analog-to-digital converter (ADC) with a maximum 5 V supply voltage for testing both methods.

The quantized terminal voltage, V_Q, is calculated by,

$$V_Q = \left\lfloor \frac{V_T}{\Delta V_Q} + 0.5 \right\rfloor \times \Delta V_Q \tag{29}$$

where V_T is the measured terminal voltage and ΔV_Q is the quantization step size, defined as,

$$\Delta V_Q = \frac{V_{max}}{2^n - 1}$$

Here, V_{max} represents the maximum voltage (5 V) that the ADC can measure and n is the resolution of the ADC, which determines the number of distinct levels (1024 for a 10-bit ADC). The impact of quantization error introduced by the ADC is depicted in Fig. 18, ranging from −2.44 mV to 2.44 mV. This variability in error magnitude correlates with the dynamics of the terminal voltage.

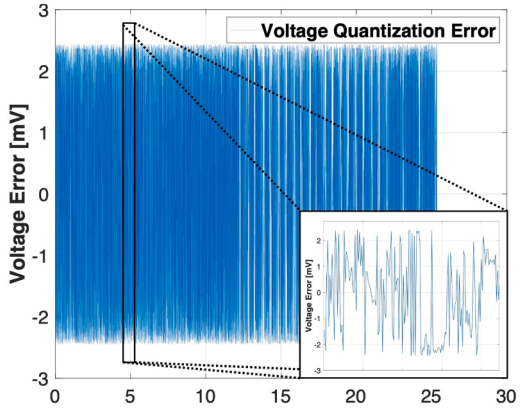

Fig. 18. Voltage quantization error added in the test.

The test results are displayed in Fig. 19. We observe that the voltage quantization error does not significantly impact either method. The RMSE for the proposed method and the UKF are 2.69 % and 7.1325 %, respectively. These errors are only slightly higher than those obtained without the presence of voltage quantization errors. This minimal impact is attributed to the distribution of the quantization error due to the dynamic nature of the voltage changes. As illustrated in Fig. 20, the voltage quantization errors are almost uniformly distributed with a zero-mean value. Since there is no constant voltage bias introduced by the ADC, these uniformly distributed measurement errors are effectively managed by both methods.

3.7. Prolonged operation in soc-ocv flat zones with low temperature

In this subsection, we evaluate the performance of the proposed method and the UKF within the SOC—OCV flat zone at 10 °C. The parameters for both methods are set based on data obtained at 25 °C. Specifically, the OCV-SOC curves used for both methods and the RC parameters utilized in the UKF are derived from tests conducted at 25 °C. This setup aims to assess how well each method performs under temperatures for which they do not have directly associated parameters.

The test results are presented in Fig. 21. The RMSE for the proposed method and the UKF are 3.28 % and 28.11 %, respectively. The UKF exhibits a peak error of up to 65 %, primarily because its performance heavily depends on the accuracy of the RC parameters. When using RC parameters calibrated at 25 °C, significant discrepancies arise at 10 °C, akin to substantial offset errors in the model. The UKF struggles to manage these discrepancies as Gaussian-distributed process noise. Conversely, the proposed method is less impacted by the temperature change because it primarily relies on the OCV-SOC relationship, which is less sensitive to temperature variations compared to the RC parameters. Moreover, parameters are estimated in real-time via the *Parameter*

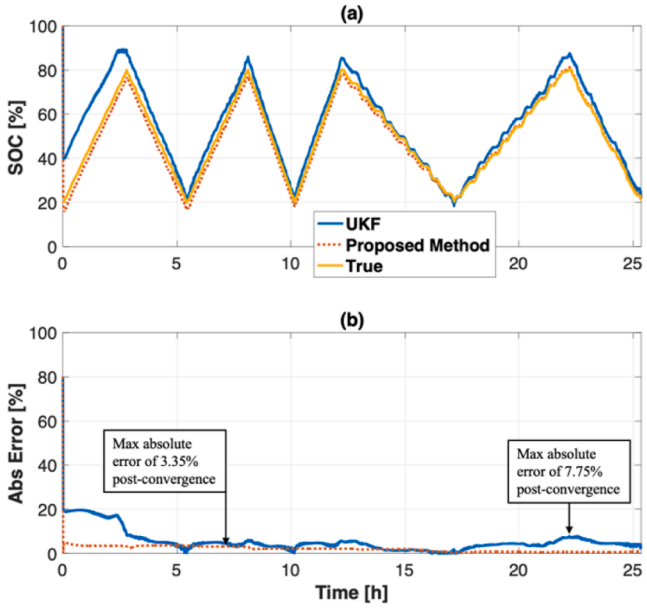

Fig. 19. Test results of the SOC—OCV flat zone with voltage quantization errors. The operation is from 20 % to 80 % SOC at 25 °C with four different current profiles and 10-bit ADC with a maximum 5 V supply voltage. (a) SOC comparison between the UKF, proposed method, and true SOC. (b) Absolute error (%) comparison, showing a maximum absolute error of 3.35 % for the proposed method and 7.75 % for the UKF after convergence. The RMSE values are 2.69 % and 7.1325 % for the proposed method and UKF, respectively.

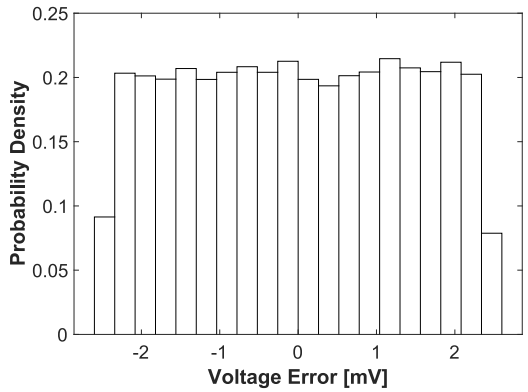

Fig. 20. Distribution of the voltage quantization error added in the test.

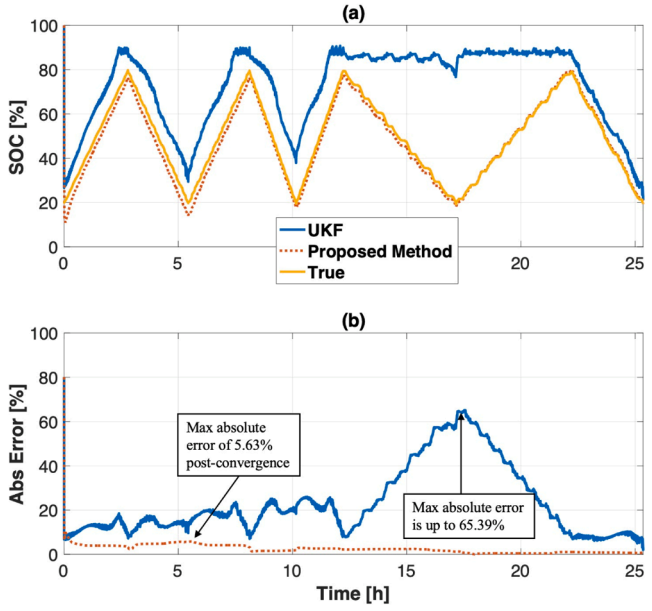

Fig. 21. Test results of the SOC—OCV flat zone and low temperature. The operation is from 20 % to 80 % SOC at 10 °C with four different current profiles. (a) SOC comparison between the UKF, proposed method, and true SOC. (b) Absolute error (%) comparison, showing a maximum absolute error of 5.63 % for the proposed method and 65.39 % for the UKF after convergence. The RMSE values are 3.28 % and 28.11 % for the proposed method and UKF, respectively.

Estimation Module in Section II.B.

As depicted in the upper plot of Fig. 22, the LFP cell's OCV-SOC curves are very similar across different temperatures. This similarity might lead readers to question why the proposed method does not perform as well at 10 °C as it does at 25 °C. The answer is intricately linked to the flat zone of the OCV-SOC curve for the LFP cell. For a given OCV value, we calculated the SOC differences between 10 °C and 25 °C from both the discharge and charge curves. As illustrated in the lower plot of Fig. 22, within the flat zone, these SOC differences at a given OCV are still substantial, posing a challenge for accurately determining the SOC at 10 °C using the 25 °C OCV-SOC relationship. However, this issue can be effectively addressed in practical applications by incorporating temperature as an input factor and using a temperature-adaptive OCV-H-SOC relationship.

3.8. *Operation in soc-ocv flat zones with a long constant current segment*

The last test aims to verify the ability of the proposed system to handle conditions with insufficient current excitation. Unlike online

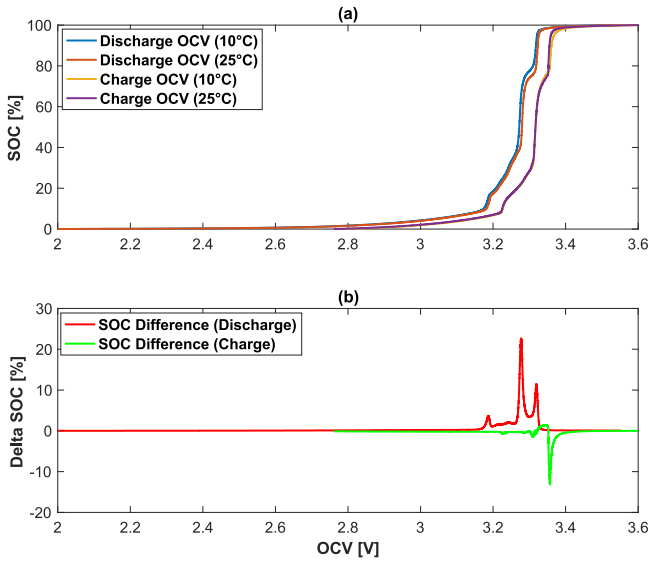

Fig. 22. OCV-SOC relationship of an LFP cell at 10 °C and 25 °C. (a) Discharge and charge OCV curves at 10 °C and 25 °C. (b) SOC differences due to temperature variations: the red line shows SOC differences between 10 °C and 25 °C at given discharging OCV values, while the green line shows SOC differences between 10 °C and 25 °C at given charging OCV values.

parameter estimation methods, the UKF, as a model-based method with predefined parameters, does not have these limitations. Therefore, it is not included in this discussion. In the test, the initial SOC guess was set at 100 %, while the true SOC was 80 %, introducing a 20 % initial error. The battery was discharged from 80 % SOC to 20 % SOC and then charged back to 80 % SOC, keeping the operation within the SOC—OCV flat zone at 25 °C. More importantly, a 15-minute constant charging current segment (−1 A) was included and is highlighted in Fig. 23.

As shown in the lower subplot of Fig. 24, the RMSE of the proposed method is 2.96 %. Remarkably, the SOC_{est} matches the true SOC even during the constant current segment. Besides, we can see that once the constant current is applied, leading to a low current excitation level, the value of SOC_{OCV-H} for the Parameter Estimation Module becomes unreliable. However, the value of $cov_{SOC_{OCV-H}}$ also instantaneously increases. Recalling Eq. (20) in the Condition Evaluation Module, when the current excitation level is low, the first element in the inverse Fisher information matrix ($\left[F(k)^{-1}\right]_{11}$) increases, leading to a high $cov_{SOC_{OCV-H}}$

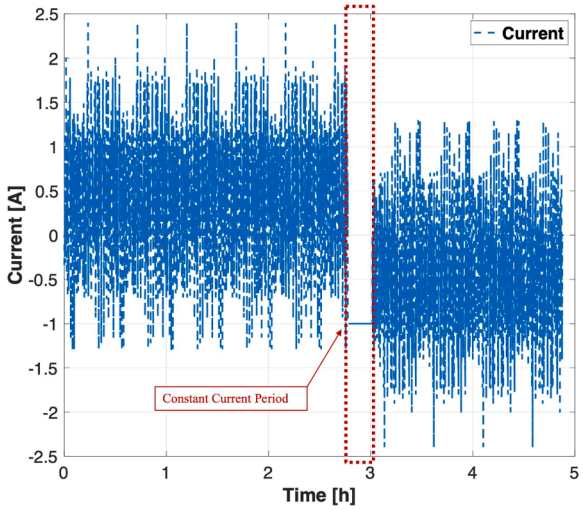

Fig. 23. Current profile with a 15-min constant current segment.

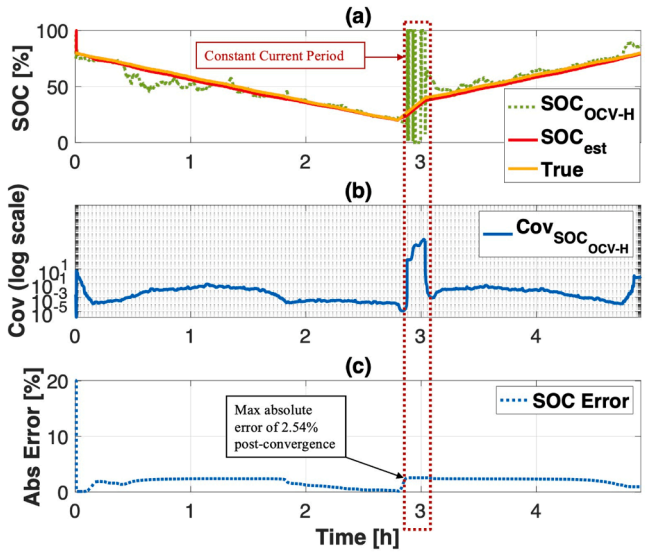

Fig. 24. Proposed method with current profile including a 15-min constant current segment.

value. Thus, with the extremely high $cov_{SOC_{OCV-H}}$ value, the SOC Fusion Module ignores the incorrect SOC_{OCV-H} value due to the constant current and relies purely on Coulomb counting to maintain more reasonable results. This demonstrates how the proposed method exhibits robustness to operating scenarios where the persistence of excitation condition is not satisfied.

4. Conclusion and discussions

4.1. Conclusion

This paper presents an adaptive and information-aware SOC estimation framework for LFP batteries, targeting fundamental challenges arising from flat SOC–OCV characteristics, pronounced hysteresis, and non-ideal operating conditions. The proposed approach introduces three key contributions:

(1) a Fisher-information-based adaptive SOC fusion strategy that dynamically balances Coulomb counting and voltage-based SOC estimation according to excitation conditions and SOC–OCV observability
(2) a hysteresis-aware three-dimensional OCV–H–SOC inversion framework for reliable SOC estimation within extended flat voltage regions
(3) a linear-in-parameter formulation that decouples OCV estimation from current measurement bias, improving robustness under biased current sensing.

Extensive experimental validation on an LFP cell using multiple realistic driving cycles demonstrates the effectiveness of the proposed framework under a wide range of challenging scenarios, including prolonged operation in SOC–OCV flat zones, large initial SOC errors, current measurement bias, voltage quantization noise, low-temperature operation, and insufficient current excitation. Compared with the unscented Kalman filter, the proposed method consistently achieves substantially lower SOC estimation errors. Notably, the RMSE is reduced from 3.92 % to 0.49 % under ideal conditions, from 6.69 % to 2.54 % during prolonged flat-zone operation, and from 15.44 % to 2.99 % in the presence of significant current bias. Even under low-temperature conditions where model mismatch severely degrades UKF performance, the proposed method maintains robust accuracy with an RMSE of 3.28 %.

Comparative results further show that while data-driven benchmarks such as LSTM and Transformer can achieve reasonable accuracy under nominal conditions, their robustness under non-ideal operating scenarios is inferior to the proposed method [56]. In particular, under low-temperature operation, the proposed framework achieves an RMSE of 3.28 %, compared with 11.42 % for LSTM and 9.95 % for the Transformer. Under significant current measurement bias, the RMSE is reduced to 2.99 %, versus 8.19 % and 9.58 % for LSTM and Transformer-based approaches, respectively. These results demonstrate that the proposed framework provides a robust, adaptive, and computationally efficient solution for real-time SOC estimation in modern LFP battery management systems.

4.2. Discussions

The proposed SOC estimation method significantly enhances estimation reliability under challenging conditions such as flat SOC–OCV regions, sensor bias, and temperature variations. By maintaining accurate SOC tracking, it improves operational safety by preventing overcharge and deep discharge, while enabling more reliable range estimation and energy management [57,58]. Beyond conventional automotive applications, accurate and reliable SOC estimation is critical for emerging and safety-critical systems. In particular, the proposed framework is well suited for electric vertical takeoff and landing (eVTOL) platforms [59], where highly dynamic power demands, strict safety margins, and limited tolerance for estimation errors necessitate condition-aware and robust SOC estimation. The ability to adaptively regulate voltage-based correction according to real-time observability is especially valuable under such operating conditions.

The proposed method is also attractive for stationary energy storage systems and second-life battery applications [60], where aging-induced parameter uncertainty, hysteresis variation, and cell-to-cell heterogeneity pose significant challenges for conventional SOC estimators. By combining online parameter adaptation, hysteresis-aware SOC inversion, and information-based confidence evaluation, the proposed framework enables reliable SOC estimation without manual recalibration, supporting higher utilization efficiency and extended battery lifetime.

Given its real-time parameter adaptation capability, the proposed framework also shows potential for extension to battery SOH [61] estimation under challenging operating conditions [62]. Future work will investigate joint SOC–SOH estimation and temperature-adaptive OCV–H–SOC mapping. While the proposed method explicitly mitigates current measurement bias, addressing voltage sensor bias through calibration, redundancy, or adaptive compensation strategies remains an important direction. In addition, improving cybersecurity resilience for battery management systems represents a promising avenue as smart energy systems continue to evolve [63].

CRediT authorship contribution statement

Junzhe Shi: Writing – review & editing, Writing – original draft, Visualization, Validation, Supervision, Software, Resources, Project administration, Methodology, Investigation, Funding acquisition, Formal analysis, Data curation, Conceptualization. **Shida Jiang:** Writing – review & editing, Writing – original draft, Visualization, Validation, Supervision, Software, Resources, Project administration, Methodology, Investigation, Funding acquisition, Formal analysis, Data curation, Conceptualization. **Shengyu Tao:** Writing – review & editing, Writing – original draft, Visualization, Validation, Supervision, Software, Resources, Project administration, Methodology, Investigation, Funding acquisition, Formal analysis, Data curation, Conceptualization. **Jaewong Lee:** Writing – review & editing, Writing – original draft, Visualization, Validation, Supervision, Software, Resources, Project administration, Methodology, Investigation, Funding acquisition, Formal analysis, Data curation, Conceptualization. **Manashita Borah:** Writing – review & editing, Writing – original draft, Visualization,

Validation, Supervision, Software, Resources, Project administration, Methodology, Investigation, Funding acquisition, Formal analysis, Data curation, Conceptualization. **Scott Moura:** Writing – review & editing, Writing – original draft, Visualization, Validation, Supervision, Software, Resources, Project administration, Methodology, Investigation, Funding acquisition, Formal analysis, Data curation, Conceptualization.

Declaration of competing interest

The authors declare that they have no known competing financial interests or personal relationships that could have appeared to influence the work reported in this paper.

Appendix

A. **Derivation of the Linear-in-Parameter Battery Model**

To facilitate real-time parameter estimation, we reformulate the second-order equivalent circuit model of the battery into a linear-in-parameter structure. The original ECM includes an open-circuit voltage (OCV), an ohmic resistance $R0$, and two RC pairs characterized by R_1 and R_2, respectively.

The voltage dynamics across each RC branch are given by the differential equations:

$$\dot{V_1}(t) = -\frac{1}{R_1 C_1} V_1(t) + \frac{I(t)}{C_1} \tag{A1}$$

$$\dot{V_2}(t) = -\frac{1}{R_2 C_2} V_2(t) + \frac{I(t)}{C_2} \tag{A2}$$

Taking the Laplace transform and solving for $V_1(s)$ and $V_2(s)$:

$$V_1(s) = \frac{R_1}{(R_1 C_1 s + 1)} I(s) \tag{A3}$$

$$V_2(s) = \frac{R_2}{(R_2 C_2 s + 1)} I(s) \tag{A4}$$

The terminal voltage in the Laplace domain is:

$$V_T(s) = OCV - R_0 I(s) - V_1(s) - V_2(s) \tag{A5}$$

Substituting the expressions for $V_1(s)$ and $V_2(s)$:

$$V_T(s) = OCV - R_0 I(s) - \frac{R_1}{(R_1 C_1 s + 1)} I(s) - \frac{R_2}{(R_2 C_2 s + 1)} I(s) \tag{A6}$$

Where:

$R_1 C_1 = \tau_1$, $R_2\, C_2 = \tau_2$

Multiplying both sides by the common denominator $(\tau_1 s + 1)(\tau_2 s + 1)$ yields:

$$\begin{aligned} &\tau_1 \tau_2 s^2 V_T(s) + (\tau_1 + \tau_2) s V_T(s) + V_T(s) = \left(\tau_1 \tau_2 s^2 + (\tau_1 + \tau_2) s + 1\right) OCV \\ &-\left(\tau_1 \tau_2 s^2 + (\tau_1 + \tau_2) s + 1\right) R_0 I(s) - R_1 (\tau_2 s + 1) I(s) - R_2 (\tau_1 s + 1) I(s) \end{aligned} \tag{A7}$$

Note that during Laplace-domain manipulation, terms involving $s^2 OCV$ and $sOCV$ naturally drop out because OCV is treated as a constant within each identification step (i.e., its derivatives are zero). Thus, only constant OCV remains in the final time-domain representation.

Rearranging to isolate $V_T(s)$ on the left and grouping by powers of s gives the convenient form:

$$\begin{aligned} V_T(s) = OCV - \tau_1 \tau_2 R_0 s^2 I(s) - (R_0 \tau_1 + R_0 \tau_2 + R_1 \tau_2 + R_2 \tau_1) s I(s) - (R_0 + R_1 + R_2) I(s) \\ -\tau_1 \tau_2 s^2 V_T(s) - (\tau_1 + \tau_2) s V_T(s) \end{aligned} \tag{A8}$$

For compact representation, we have:

$$V_T(s) = OCV - a s^2 I(s) - b s I(s) - c I(s) - d s^2 V_T(s) - e s V_T(s) \tag{A9}$$

Where the coefficients are defined as:

$$\begin{cases} a = \tau_1 \tau_2 R_0 \\ b = R_0 \tau_1 + R_0 \tau_2 + R_1 \tau_2 + R_2 \tau_1 \\ c = R_0 + R_1 + R_2 \\ d = \tau_1 \tau_2 \\ e = \tau_1 + \tau_2 \end{cases} \tag{A10}$$

Applying the inverse Laplace transform and using the correspondence $(sX(s) \longleftrightarrow \dot{x}(t))$ and $s^2 X(s) \longleftrightarrow \ddot{x}(t))$, we obtain:

$$V_T(t) = OCV - a\ddot{I}(t) - b\dot{I}(t) - cI(t) - d\ddot{V_T}(t) - e\dot{V_T}(t) \tag{A11}$$

This can be rearranged into a linear-in-parameter form:

$$V_T = [\,OCV \quad a \quad b \quad c \quad d \quad e\,] \begin{bmatrix} 1 \\ -\dddot{I} - \ddot{I} - \dot{I} - \ddot{V}_T^{\cdot} - \dot{V}_T \end{bmatrix} \tag{A12}$$

This linear form enables the use of standard linear regression techniques for real-time parameter identification. The voltage and current derivatives are computed using filtered signals as described in Appendix B.

B. Derivation of Filtered and Discretized Signal Derivatives

To support real-time parameter estimation, we extract filtered signals and their time derivatives from raw voltage and current measurements using a second-order filtering process. To estimate the filtered voltage and current signals and their time derivatives, we apply zero-order hold (ZOH) discretization to the continuous-time transfer functions $G_0(s)$, $G_1(s)$, and $G_2(s)$. These transfer functions are used to extract the signal itself, its first derivative, and its second derivative, respectively.

After ZOH discretization, we obtain the discrete-time transfer functions $G_0(z)$, $G_1(z)$, and $G_2(z)$ in the z-domain as:

$$G_2(z) = \frac{\lambda_0 (z-1)^2}{T_s^2 z^2 \left(\lambda_0 + \frac{\lambda_1 (z-1)}{T_s z} + \frac{(z-1)^2}{T_s^2 z^2} \right)} \tag{A13}$$

$$G_1(z) = \frac{\lambda_0 (z-1)}{T_s z \left(\lambda_0 + \frac{\lambda_1 (z-1)}{T_s z} + \frac{(z-1)^2}{T_s^2 z^2} \right)} \tag{A14}$$

$$G_0(z) = \frac{\lambda_0}{\lambda_0 + \frac{\lambda_1 (z-1)}{T_s z} + \frac{(z-1)^2}{T_s^2 z^2}} \tag{A15}$$

Each transfer function $G_i(z)$ (for $i = 0, 1, 2$) is then converted into a discrete-time state-space representation with system matrices A_i, B_i, C_i, D_i.

Using the state-space form, the filtered terminal voltage $\widehat{V}_T[k]$, current $\widehat{I}[k]$, and their first and second derivatives are calculated as:

Filtered Voltage:

$$x_{V_T}[k+1] = A_0 x_{V_T}(k) + B_0 V_T(k) \tag{A16}$$

$$\widehat{V}_T[k] = C_0 x_{V_T}(k) + D_0 V_T(k) \tag{A17}$$

First Derivative of Voltage:

$$x_{\dot{V}_T}[k+1] = A_1 x_{\dot{V}_T}(k) + B_1 V_T(k) \tag{A18}$$

$$\widehat{V}_T^{'}[k] = C_1 x_{\dot{V}_T}(k) + D_1 V_T(k) \tag{A19}$$

Second Derivative of Voltage:

$$x_{\ddot{V}_T}[k+1] = A_2 x_{\ddot{V}_T}(k) + B_2 V_T(k) \tag{A20}$$

$$\widehat{V}_T^{''}[k] = C_2 x_{\ddot{V}_T}(k) + D_2 V_T(k) \tag{A21}$$

Filtered Current:

$$x_I[k+1] = A_0 x_I(k) + B_0 I(k) \tag{A22}$$

$$\widehat{I}[k] = C_0 x_I(k) + D_0 I(k) \tag{A23}$$

First Derivative of Current:

$$x_{\dot{I}}[k+1] = A_1 x_{\dot{I}}(k) + B_1 I(k) \tag{A24}$$

$$\widehat{I}^{'}[k] = C_1 x_{\dot{I}}(k) + D_1 I(k) \tag{A25}$$

Second Derivative of Current:

$$x_{\ddot{I}}[k+1] = A_2 x_{\ddot{I}}(k) + B_2 I(k) \tag{A26}$$

$$\widehat{I}^{''}[k] = C_2 x_{\ddot{I}}(k) + D_2 I(k) \tag{A27}$$

C. Benchmark Comparison with Data-Driven Models (LSTM and Transformer)

Appendix C provides a comprehensive benchmarking study comparing the proposed method with leading data-driven approaches, LSTM and Transformer models, both standalone and fused with a KF. This section details the network architectures, fusion strategies, test conditions, and computational costs, and presents comparative results under a range of realistic operating scenarios. The analysis highlights the strengths and limitations of each approach, offering insights into their suitability for real-time LFP SOC estimation.

To establish a robust data-driven benchmark for SOC estimation, we implemented a deep learning model based on LSTM networks. The model was trained using real driving data collected from multiple battery test cycles. To ensure generalizability, all available valid cycles were used for training. A

comprehensive set of features was engineered, including voltage, current, their derivatives, moving averages, and instantaneous power, followed by z-score normalization. A sequence length of 120 with a stride of 8 was chosen to balance temporal resolution and computational efficiency. The architecture consisted of a bidirectional LSTM layer with 256 hidden units to capture temporal dependencies, followed by a unidirectional LSTM layer with 128 units, and a series of dense layers with dropout and batch normalization for regularization and improved convergence. The network was trained using the Adam optimizer and adaptive learning rate scheduling. This LSTM-based model provides a strong deep learning baseline that reflects the capability of sequence modeling architectures in learning SOC behavior from raw voltage and current data alone.

To enhance the robustness and accuracy of SOC estimation, we implemented a sensor fusion strategy that combines Coulomb Counting (CC) with LSTM-based predictions using a one-dimensional KF. The system dynamics model assumes SOC evolution based on CC, accounting for coulombic efficiency during charging and a small self-discharge rate, while treating the LSTM output as a noisy measurement of the true SOC. Specifically, the prediction step uses the current and battery capacity to estimate SOC incrementally, introducing process noise to capture uncertainties in CC. The correction step incorporates the LSTM-based SOC estimate when available, adjusting the state estimate based on the Kalman gain computed from process and measurement noise covariances. The filter was initialized with a small state covariance and tuned with empirically selected values for process ($Q = 10^{-7}$) and measurement ($R = 10^{-2}$) noise. The LSTM measurements are fused starting from the earliest index where sequence input becomes available. This fusion approach leverages the high-frequency consistency of CC and the learned nonlinear modeling capacity of LSTM, resulting in a more stable and accurate SOC estimate that mitigates the weaknesses of each individual source. Physical bounds were enforced throughout to ensure realistic SOC values.

We also implemented a decoder-only Transformer model with masked multi-head self-attention, tailored for real-time SOC prediction. This architecture follows the canonical Transformer decoder structure, leveraging stacked layers of masked multi-head self-attention and position-wise feedforward networks, along with residual connections and layer normalization, to capture long-range temporal dependencies in the input sequences. To ensure real-time compatibility and strict temporal causality, masked self-attention is applied in each decoder block so that the model only attends to historical and current measurements (voltage and current), never using any future information for prediction. The input to the network is a two-channel sequence (voltage and current) with a length of 120 timesteps, corresponding to a 2-minute history at 1 Hz sampling. These inputs are standardized using z-score normalization with normalization parameters recorded for deployment compatibility. The model consists of six stacked decoder blocks, each composed of masked multi-head self-attention (with 8 attention heads and model dimension of 192), feedforward layers (hidden size 384 followed by 192), dropout layers (rates ranging from 2 % to 6 %), and residual skip connections with layer normalization. The final output is generated by applying a fully connected regression head to the representation at the last timestep. The network was trained using the Adam optimizer with a learning rate of 0.0001, a mini-batch size of 12, a total of 60 epochs, and L2 regularization of 3×10^{-6}. Validation was performed using an 80/20 split of the sequences. This model provides a strong ability to capture complex nonlinear dynamics and hysteresis behavior in LFP batteries. While recurrent neural networks such as LSTMs have been more commonly used for SOC estimation, Transformer-based causal sequence models are a recent and promising approach in this domain, making this architecture a valuable and rigorous benchmark for evaluating the performance of real-time data-driven SOC estimation methods under challenging operating conditions.

To further enhance the robustness of the Transformer-based SOC predictions and reduce the inherent short-term noise observed in purely data-driven outputs, we developed a KF-based fusion approach similar to the LSTM + KF method. Here, SOC evolution is again propagated using CC, and the Transformer output is incorporated as a noisy measurement. The same KF parameters were used ($Q = 10^{-7}$, $R = 10^{-2}$, $P_0 = 10^{-2}$), and Transformer predictions are fused when available. This hybrid Transformer + KF model combines the Transformer's strong nonlinear modeling capabilities with the temporal consistency and stability of CC, producing smoother and more reliable SOC estimates while maintaining real-time compatibility.

The system architecture of the LSTM/Transformer plus KF model is presented in the Fig. A1. The model consists of an input sequence (voltage and current) that is processed through stacked LSTM layers/decoder-only Transformer model. The output provides a sequence-based SOC estimate, $SOC_{DD\ Model}$, which is then fused with Coulomb Counting through a one-dimensional Kalman Filter. The Kalman filter propagates SOC using CC as the process model and incorporates the data-driven model prediction as a noisy measurement update.

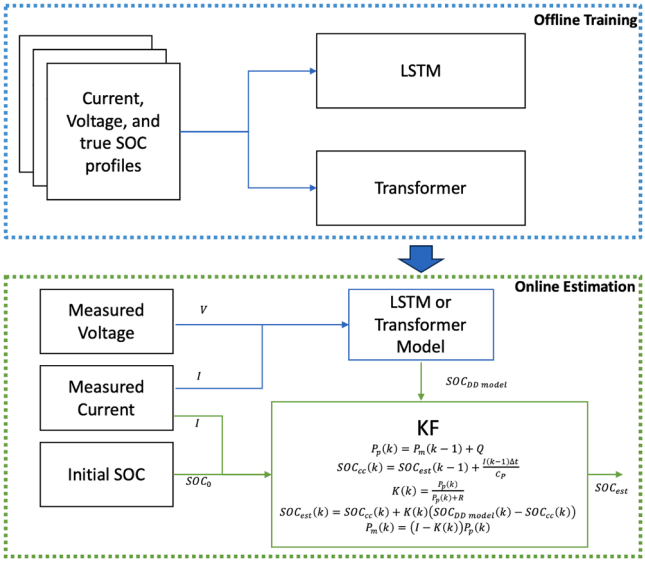

Fig. A1. System architecture of the LSTM/Transformer + KF model.

To validate the effectiveness of these methods, we conducted a comparative analysis summarized in Table A1 and Fig. A2 through Fig. A6. In

addition to the data-driven methods, we included the UKF as a reference baseline. While the UKF's structure and performance have been discussed in detail in the main body of the paper, we include its results here for completeness and comparative context.

Table A1 presents the RMSE of SOC estimation under five representative conditions: ideal case, SOC—OCV flat zone, current bias, quantization error, and low temperature. Across all cases, the proposed method consistently outperformed the benchmarks. Both Transformer + KF and LSTM + KF showed notable improvements over their standalone counterparts, validating the effectiveness of hybrid fusion.

Table A1
SOC Estimation RMSE (%) Across Different Test Conditions.

Test Condition	Proposed	UKF	LSTM	LSTM + KF	Transformer	Transformer + KF
Ideal Case	0.49 %	3.92 %	5.51 %	4.32 %	3.197 %	2.36 %
SOC—OCV Flat Zone	2.54 %	6.69 %	7.24 %	5.97 %	7.02 %	5.52 %
Constant Current Bias	2.99 %	15.44 %	8.19 %	6.77 %	9.58 %	5.86 %
Quantization Error	2.69 %	7.13 %	7.27 %	5.99 %	7.056 %	5.59 %
Low Temperature	3.28 %	28.11 %	11.42 %	8.69 %	9.95 %	8.29 %

Table A2 reports the computational cost of each method per prediction. All computations were performed on a standard laptop (Apple M1 Max, 64 GB memory). Execution times were averaged over 129,618 steps (equivalent to 36 h of operation at a 1-second sampling interval) and normalized per time step. As expected, the UKF achieved the lowest cost (0.63 ms) due to its lightweight structure. The LSTM- and Transformer-based models required more computation (1.31 ms and 1.78 ms, respectively) owing to their deeper neural network architectures. Notably, augmenting these models with a Kalman Filter introduced only minimal additional overhead, approximately 0.005 ms, while substantially improving robustness and accuracy under challenging test conditions. The proposed method, which incorporates interpolation and regression modules, achieved a balanced runtime of 1.17 ms. All methods remain well within acceptable limits for real-time onboard SOC estimation, and the fusion strategies (LSTM + KF and Transformer + KF) represent a compelling trade-off between performance and computational efficiency.

Table A2
Computational Cost per Prediction.

	Proposed	UKF	LSTM	LSTM + KF	Transformer	Transformer + KF
Operation time	1.17 ms	0.63 ms	1.31 ms	1.32 ms	1.78 ms	1.79 ms

Under the ideal test condition (Fig. A2), all models achieved relatively low errors. The proposed method yielded the best performance, followed by Transformer + KF (2.36 %). The Transformer's ability to model long-term patterns and the KF's grounding in physical dynamics created a complementary effect. Notably, Transformer outperformed LSTM even as a standalone method, highlighting its strength in capturing global sequence structures.

In the SOC—OCV flat zone (Fig. A3), the estimation challenge increased due to poor observability from voltage signals—a characteristic limitation of LFP chemistry. All models experienced degraded performance, particularly the UKF, which relies on voltage for state correction. However, the fusion-based models (Transformer + KF and LSTM + KF) maintained better accuracy by leveraging current integration from CC to supplement the limited information from voltage.

In the constant current bias scenario (Fig. A4), the UKF performed poorly due to its dependence on direct current measurements and the resultant accumulation of integration errors under bias. Purely data-driven models such as Transformer and LSTM were more robust to current bias, owing to their learned sequence representations, but still exhibited prediction drift in the absence of physical correction. The fusion approaches also degraded in this setting, as the integrated CC model was itself affected by the bias-induced drift, limiting the effectiveness of the Kalman correction.

For quantization error (Fig. A5), fusion again proved beneficial. While voltage quantization reduced the resolution of observable dynamics, CC-based models smoothed over the noise, and LSTM + KF and Transformer + KF achieved robust performance (5.99 % and 5.59 %, respectively). This case illustrates that voltage quantization errors introduced by ADCs can be mitigated if appropriately filtered in all methods.

At low temperatures (Fig. A6), all methods deteriorated, with UKF showing the largest error (28.11 %) due to unmodeled temperature-dependent behaviors. Data-driven models also degraded, highlighting their sensitivity to out-of-distribution conditions. Fusion strategies showed better generalization (8.69 % and 8.29 % for LSTM + KF and Transformer + KF, respectively) but still lagged behind the proposed method (3.28 %).

In summary, while deep learning models such as LSTM and Transformer can capture complex, nonlinear battery behaviors and achieve high accuracy on representative datasets, they struggle to generalize under distribution shifts, sensor noise, or operating conditions not seen during training. Their lack of physical constraints can lead to prediction drift and unrealistic SOC estimates. By fusing these models with physically grounded CC via a Kalman Filter, both robustness and interpretability are improved, resulting in more stable and physically plausible predictions. Although these hybrid approaches still trail the proposed physics-informed method in overall performance, they offer strong, real-time-capable benchmarks for SOC estimation. Future work could explore incorporating additional physical variables, such as temperature, or applying domain adaptation and online recalibration to further enhance the generalization ability of data-driven models.

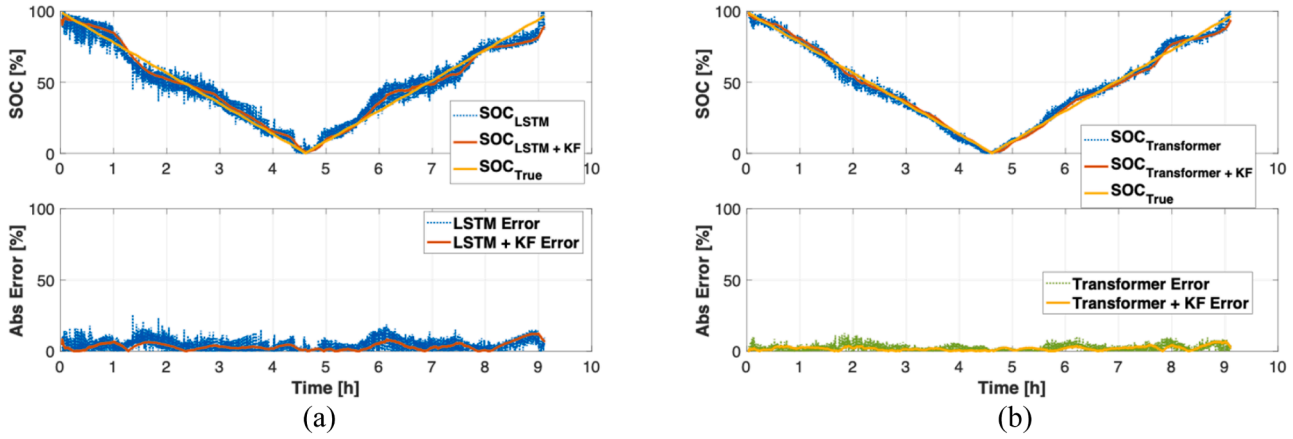

Fig. A2. Test results under ideal condition. (a) LSTM & LSTM + Kalman filter. (b) Transformer & Transformer + Kalman filter.

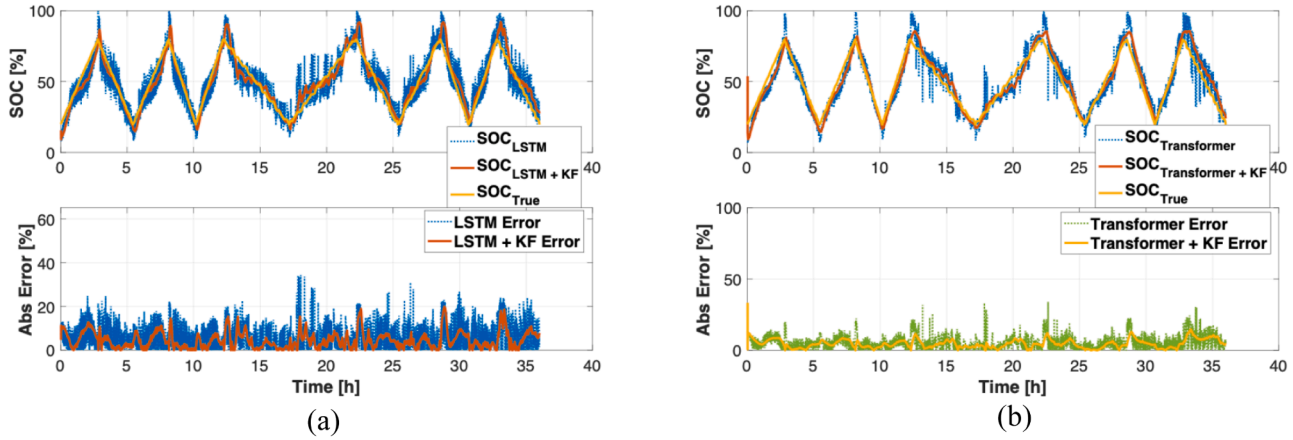

Fig. A3. Test results of the SOC—OCV flat zone. (a) LSTM & LSTM + Kalman filter. (b) Transformer & Transformer + Kalman filter.

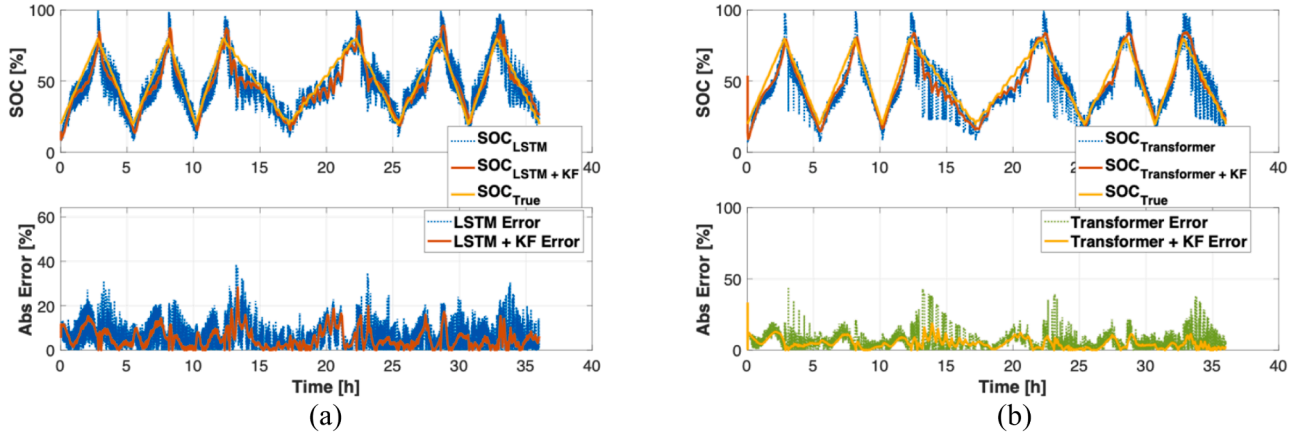

Fig. A4. Test results of the SOC—OCV flat zone adding a high current measurement bias (−0.05A). (a) LSTM & LSTM + Kalman filter. (b) Transformer & Transformer + Kalman filter.

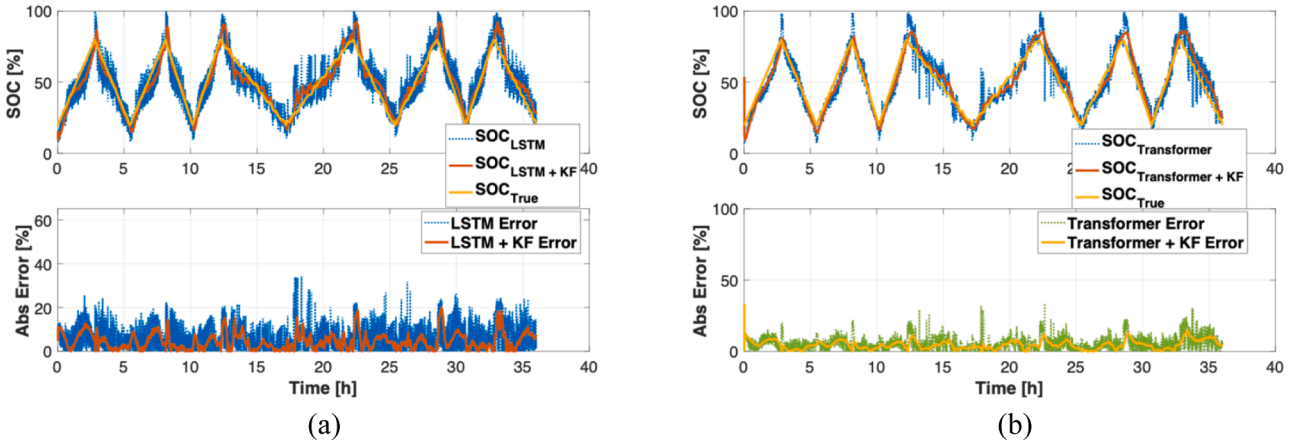

Fig. A5. Test results of the SOC—OCV flat zone with voltage quantization errors (10-bit ADC). (a) LSTM & LSTM + Kalman filter. (b) Transformer & Transformer + Kalman filter.

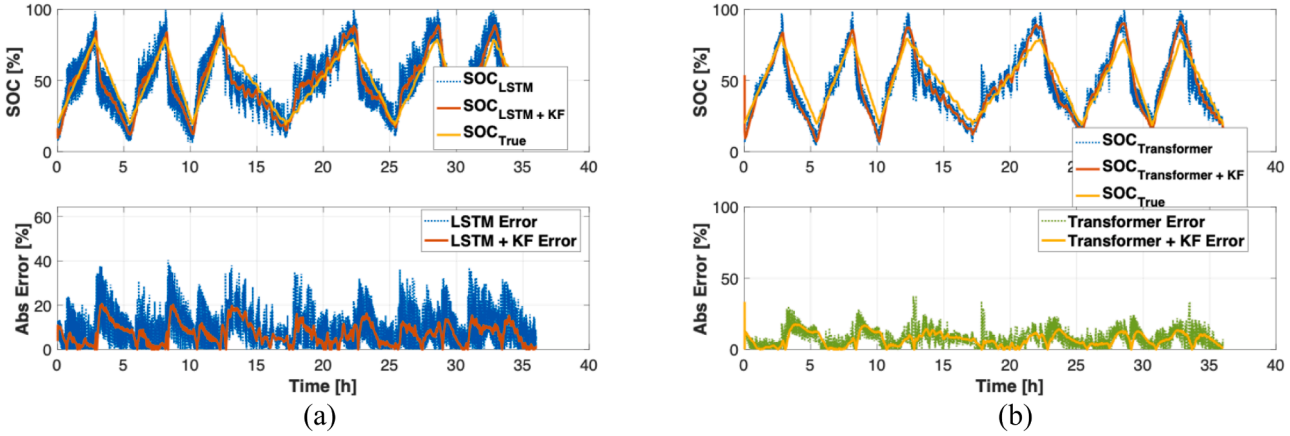

Fig. A6. Test results of the SOC—OCV flat zone and low temperature (10 °C). (a) LSTM & LSTM + Kalman filter. (b) Transformer & Transformer + Kalman filter.

Data availability

Data will be made available on request.

References

[1] Demirci O, Taskin S, Schaltz E, Demirci BAcar. Review of battery state estimation methods for electric vehicles - part I: SOC estimation. J Energy Storage 2024;87:111435. https://doi.org/10.1016/j.est.2024.111435.

[2] Shi J, Xu B, Shen Y, Wu J. Energy management strategy for battery/supercapacitor hybrid electric city bus based on driving pattern recognition. Energy 2021:122752. https://doi.org/10.1016/j.energy.2021.122752.

[3] Chen D, Kim Y, Stefanopoulou AG. Predictive equivalent consumption minimization strategy with segmented traffic information. IEEE Trans Veh Technol 2020;69(12):14377–90. https://doi.org/10.1109/TVT.2020.3034552.

[4] Shi J, Tian M, Han S, Wu T-Y, Tang Y. Electric vehicle battery remaining charging time estimation considering charging accuracy and charging profile prediction. J Energy Storage 2022;49:104132. https://doi.org/10.1016/j.est.2022.104132.

[5] Shi J, Zeng T, Moura S. The nature and strategy of minimizing the total travel time for long-distance driving of an EV. IEEE Trans Transp Electrif 2024. https://doi.org/10.1109/TTE.2024.3365009. pp. 1–1.

[6] Lin C, Yu Q, Xiong R, Wang LY. A study on the impact of open circuit voltage tests on state of charge estimation for lithium-ion batteries. Appl Energy 2017;205:892–902. https://doi.org/10.1016/j.apenergy.2017.08.124.

[7] Mao S, et al. Multi sensor fusion methods for state of charge estimation of smart lithium-ion batteries. J Energy Storage 2023;72:108736. https://doi.org/10.1016/j.est.2023.108736.

[8] Shi J, Kato D, Jiang S, Dangwal C, Moura S. Robust estimation of State of charge in lithium iron phosphate cells enabled by online parameter estimation and deep neural networks. IFAC-Pap 2023;56(3):127–32. https://doi.org/10.1016/j.ifacol.2023.12.012.

[9] Wu L, Lyu Z, Huang Z, Zhang C, Wei C. Physics-based battery SOC estimation methods: recent advances and future perspectives. J Energy Chem 2024;89:27–40. https://doi.org/10.1016/j.jechem.2023.09.045.

[10] Gao Y, Nguyen T, Onori S. Model-based State-of-charge estimation of 28 V $LiFePO_4$ aircraft battery. SAE Int J Elec Veh 2024;14(1). https://doi.org/10.4271/14-14-01-0003. Art. no. 14-14-01–0003.

[11] Wu L, Liu K, Pang H. Evaluation and observability analysis of an improved reduced-order electrochemical model for lithium-ion battery. Electrochim Acta 2021;368:137604. https://doi.org/10.1016/j.electacta.2020.137604.

[12] He Z, Yang Z, Cui X, Li E. A method of State-of-charge estimation for EV power lithium-ion battery using a novel adaptive extended kalman filter. IEEE Trans Veh Technol 2020;69(12):14618–30. https://doi.org/10.1109/TVT.2020.3032201.

[13] Hossain M, Haque ME, Arif MT. Kalman filtering techniques for the online model parameters and state of charge estimation of the Li-ion batteries: a comparative analysis. J Energy Storage 2022;51:104174. https://doi.org/10.1016/j.est.2022.104174.

[14] S. Jiang, J. Shi, and S. Moura, "A new framework for nonlinear Kalman filters," 2024, *arXiv*: arXiv:2407.05717. doi: 10.48550/arXiv.2407.05717.

[15] S. Jiang, J. Shi, M. Borah, and S. Moura, "Weaknesses and Improvements of the Extended Kalman Filter for Battery State-of-Charge and State-of-Health Estimation," in *2024 American Control Conference (ACC)*, 2024, pp. 1441–8. doi: 10.23919/ACC60939.2024.10644628.

[16] Gao Y, Plett GL, Fan G, Zhang X. Enhanced state-of-charge estimation of LiFePO4 batteries using an augmented physics-based model. J Power Sources 2022;544:231889. https://doi.org/10.1016/j.jpowsour.2022.231889.

[17] Wang S, Zhang S, Wen S, Fernandez C. An accurate state-of-charge estimation of lithium-ion batteries based on improved particle swarm optimization-adaptive square root cubature kalman filter. J Power Sources 2024;624:235594. https://doi.org/10.1016/j.jpowsour.2024.235594.

[18] Maheshwari A, Nageswari S. Effect of noise covariance matrices on State of charge estimation using extended kalman filter. IETE J Res 2023;69(11):8130–41. https://doi.org/10.1080/03772063.2022.2055657.

[19] Song Y, Liu D, Liao H, Peng Y. A hybrid statistical data-driven method for on-line joint state estimation of lithium-ion batteries. Appl Energy 2020;261:114408. https://doi.org/10.1016/j.apenergy.2019.114408.

[20] Li Y, Ye M, Wang Q, Lian G, Xia B. An improved model combining machine learning and Kalman filtering architecture for state of charge estimation of lithium-ion batteries. Green Energy Intell Transp 2024;3(4):100163. https://doi.org/10.1016/j.geits.2024.100163.
[21] Hammou A, Petrone R, Gualous H, Diallo D. Deep learning framework for state of health estimation of NMC and LFP Li-ion batteries for vehicular applications. J Energy Storage 2023;70:108083. https://doi.org/10.1016/j.est.2023.108083.
[22] Hossain Lipu MS, et al. Data-driven state of charge estimation of lithium-ion batteries: algorithms, implementation factors, limitations and future trends. J Clean Prod 2020;277:124110. https://doi.org/10.1016/j.jclepro.2020.124110.
[23] Liu M, Xu J, Jiang Y, Mei X. Multi-dimensional features based data-driven state of charge estimation method for LiFePO4 batteries. Energy 2023;274:127407. https://doi.org/10.1016/j.energy.2023.127407.
[24] Yang F, Song X, Xu F, Tsui K-L. State-of-charge estimation of lithium-ion batteries via long short-term memory network. IEEE Access 2019;7:53792–9. https://doi.org/10.1109/ACCESS.2019.2912803.
[25] Shen H, Zhou X, Wang Z, Wang J. State of charge estimation for lithium-ion battery using Transformer with immersion and invariance adaptive observer. J Energy Storage 2022;45:103768. https://doi.org/10.1016/j.est.2021.103768.
[26] Wei M, Ye M, Zhang C, Lian G, Xia B, Wang Q. Robust state of charge estimation of LiFePO4 batteries based on Sage_Husa adaptive Kalman filter and dynamic neural network. Electrochim Acta 2024;477:143778. https://doi.org/10.1016/j.electacta.2024.143778.
[27] Tao S, et al. Collaborative and privacy-preserving retired battery sorting for profitable direct recycling via federated machine learning. Nat Commun 2023;14(1):8032. https://doi.org/10.1038/s41467-023-43883-y.
[28] Tao S, et al. Battery cross-operation-condition lifetime prediction via interpretable feature engineering assisted adaptive machine learning. ACS Energy Lett 2023;8(8):3269–79. https://doi.org/10.1021/acsenergylett.3c01012.
[29] Ma R, et al. Pathway decisions for reuse and recycling of retired lithium-ion batteries considering economic and environmental functions. Nat Commun 2024;15(1):7641. https://doi.org/10.1038/s41467-024-52030-0.
[30] Tao S, et al. The proactive maintenance for the irreversible sulfation in lead-based energy storage systems with a novel resonance method. J Energy Storage 2021;42:103093. https://doi.org/10.1016/j.est.2021.103093.
[31] He K, et al. A novel quick screening method for the second usage of parallel-connected lithium-ion cells based on the current distribution. J Electrochem Soc 2023;170(3):030514. https://doi.org/10.1149/1945-7111/acbf7e.
[32] Tao S, et al. Non-destructive degradation pattern decoupling for early battery trajectory prediction via physics-informed learning. Energy Env Sci 2025;18(3):1544–59. https://doi.org/10.1039/D4EE03839H.
[33] Tao S, et al. Generative learning assisted state-of-health estimation for sustainable battery recycling with random retirement conditions. Nat Commun 2024;15(1):10154. https://doi.org/10.1038/s41467-024-54454-0.
[34] Tao S, et al. PulseBat: a field-accessible dataset for second-life battery diagnostics from realistic histories using multidimensional rapid pulse test. Nat Commun 2024;15(1):10154. https://doi.org/10.1038/s41467-024-54454-0.
[35] Xu R, de Vasconcelos LS, Shi J, Li J, Zhao K. Disintegration of Meatball electrodes for LiNixMnyCozO2 cathode materials. Exp Mech 2018;58(4):549–59. https://doi.org/10.1007/s11340-017-0292-0.
[36] Mehta C, Sant AV, Sharma P. Optimized ANN for LiFePO4 battery charge estimation using principal components based feature generation. Green Energy Intell Transp 2024;3(4):100175. https://doi.org/10.1016/j.geits.2024.100175.
[37] Xiong R, Duan Y, Zhang K, Lin D, Tian J, Chen C. State-of-charge estimation for onboard LiFePO4 batteries with adaptive state update in specific open-circuit-voltage ranges. Appl Energy 2023;349:121581. https://doi.org/10.1016/j.apenergy.2023.121581.
[38] Jöst D, Palaniswamy LN, Quade KL, Sauer DU. Towards robust state estimation for LFP batteries: model-in-the-loop analysis with hysteresis modelling and perspectives for other chemistries. J Energy Storage 2024;92:112042. https://doi.org/10.1016/j.est.2024.112042.
[39] Wang S, Wang C, Takyi-Aninakwa P, Jin S, Fernandez C, Huang Q. An improved parameter identification and radial basis correction-differential support vector machine strategies for state-of-charge estimation of urban-transportation-electric-vehicle lithium-ion batteries. J Energy Storage 2024;80:110222. https://doi.org/10.1016/j.est.2023.110222.
[40] Wang S, Dang Q, Gao Z, Li B, Fernandez C, Blaabjerg F. An innovative square root - untraced Kalman filtering strategy with full-parameter online identification for state of power evaluation of lithium-ion batteries. J Energy Storage 2024;104:114555. https://doi.org/10.1016/j.est.2024.114555.
[41] Montgomery DC, Peck EA, Vining GG. Introduction to linear regression analysis. John Wiley & Sons; 2021.
[42] Mohamed MAA, Yu TF, Ramsden G, Marco J, Grandjean T. Advancements in parameter estimation techniques for 1RC and 2RC equivalent circuit models of lithium-ion batteries: a comprehensive review. J Energy Storage 2025;113:115581. https://doi.org/10.1016/j.est.2025.115581.
[43] Dvorak D, Bäuml T, Holzinger A, Popp H. A comprehensive algorithm for estimating lithium-ion battery parameters from measurements. IEEE Trans Sustain Energy 2018;9(2):771–9. https://doi.org/10.1109/TSTE.2017.2761406.
[44] Ovejas VJ, Cuadras A. State of charge dependency of the overvoltage generated in commercial Li-ion cells. J Power Sources 2019;418:176–85. https://doi.org/10.1016/j.jpowsour.2019.02.046.
[45] Pozzato G, Li X, Lee D, Ko J, Onori S. Accelerating the transition to cobalt-free batteries: a hybrid model for LiFePO4/graphite chemistry. npj Comput Mater 2024;10(1):1–12. https://doi.org/10.1038/s41524-024-01197-7.
[46] Li Y, et al. Current-induced transition from particle-by-particle to concurrent intercalation in phase-separating battery electrodes. Nat Mater 2014;13(12):1149–56. https://doi.org/10.1038/nmat4084.
[47] Barai A, Widanage WD, Marco J, McGordon A, Jennings P. A study of the open circuit voltage characterization technique and hysteresis assessment of lithium-ion cells. J Power Sources 2015;295:99–107. https://doi.org/10.1016/j.jpowsour.2015.06.140.
[48] Jahn L, Mößle P, Röder F, Danzer MA. A physically motivated voltage hysteresis model for lithium-ion batteries using a probability distributed equivalent circuit. Commun Eng 2024;3(1):1–11. https://doi.org/10.1038/s44172-024-00221-4.
[49] Kwak M, Lkhagvasuren B, Park J, You J-H. Parameter identification and SOC estimation of a battery under the hysteresis effect. IEEE Trans Ind Electron 2020;67(11):9758–67. https://doi.org/10.1109/TIE.2019.2956394.
[50] C.P. Graells, M.S. Trimboli, and G.L. Plett, "Differential hysteresis models for a silicon-anode Li-ion battery cell," in *2020 IEEE Transportation Electrification Conference & Expo (ITEC)*, 2020, pp. 175–80. doi: 10.1109/ITEC48692.2020.9161591.
[51] Tran M-K, Mevawala A, Panchal S, Raahemifar K, Fowler M, Fraser R. Effect of integrating the hysteresis component to the equivalent circuit model of Lithium-ion battery for dynamic and non-dynamic applications. J Energy Storage 2020;32:101785. https://doi.org/10.1016/j.est.2020.101785.
[52] Marongiu A, Nußbaum FGW, Waag W, Garmendia M, Sauer DU. Comprehensive study of the influence of aging on the hysteresis behavior of a lithium iron phosphate cathode-based lithium ion battery – An experimental investigation of the hysteresis. Appl Energy 2016;171:629–45. https://doi.org/10.1016/j.apenergy.2016.02.086.
[53] Rothenberger MJ, Docimo DJ, Ghanaatpishe M, Fathy HK. Genetic optimization and experimental validation of a test cycle that maximizes parameter identifiability for a Li-ion equivalent-circuit battery model. J Energy Storage 2015;4:156–66. https://doi.org/10.1016/j.est.2015.10.004.
[54] Song Z, Hofmann H, Lin X, Han X, Hou J. Parameter identification of lithium-ion battery pack for different applications based on Cramer-Rao bound analysis and experimental study. Appl Energy 2018;231:1307–18. https://doi.org/10.1016/j.apenergy.2018.09.126.
[55] Lin X. Theoretical analysis of battery SOC estimation errors under sensor bias and variance. IEEE Trans Ind Electron 2018;65(9):7138–48. https://doi.org/10.1109/TIE.2018.2795521.
[56] Chen Y, Duan W, He Y, Wang S, Fernandez C. A hybrid data driven framework considering feature extraction for battery state of health estimation and remaining useful life prediction. Green Energy Intell Transp 2024;3(2):100160. https://doi.org/10.1016/j.geits.2024.100160.
[57] Shi J, Aarsnes UJF, Tao S, Wang R, Nærheim D, Moura S. Health-aware energy management for multiple stack hydrogen fuel cell and battery hybrid systems. Appl Energy 2025;397:126257. https://doi.org/10.1016/j.apenergy.2025.126257.
[58] Dong H, Shi J, Zhuang W, Li Z, Song Z. Analyzing the impact of mixed vehicle platoon formations on vehicle energy and traffic efficiencies. Appl Energy 2025;377:124448. https://doi.org/10.1016/j.apenergy.2024.124448.
[59] Yang X-G, Liu T, Ge S, Rountree E, Wang C-Y. Challenges and key requirements of batteries for electric vertical takeoff and landing aircraft. Joule 2021;5(7):1644–59. https://doi.org/10.1016/j.joule.2021.05.001.
[60] Tao S, et al. Immediate remaining capacity estimation of heterogeneous second-life lithium-ion batteries via deep generative transfer learning. Energy Env Sci 2025;18(15):7413–26. https://doi.org/10.1039/D5EE02217G.
[61] X. Huang et al., "Physics-informed mixture of experts network for interpretable battery degradation trajectory computation amid second-life complexities," 2025, *arXiv*: arXiv:2506.17755. doi: 10.48550/arXiv.2506.17755.
[62] Wei M, Ye M, Zhang C, Wang Q, Lian G, Xia B. Integrating mechanism and machine learning based capacity estimation for LiFePO4 batteries under slight overcharge cycling. Energy 2024;296:131208. https://doi.org/10.1016/j.energy.2024.131208.
[63] Shi J, Wu J, Xu B, Song Z. Cybersecurity of hybrid electric City bus with V2C connectivity. IEEE Trans Intell Veh 2023:1–16. https://doi.org/10.1109/TIV.2023.3281032.